bioRxiv preprint doi: https://doi.org/10.1101/2023.10.25.564063; this version posted October 26, 2023. The copyright holder for this preprint (which was not certified by peer review) is the author/funder, who has granted bioRxiv a license to display the preprint in perpetuity. It is made available under aCC-BY-ND 4.0 International license.

1 **Interactions between pili affect the outcome of bacterial competition**
2 **driven by the type VI secretion system**

3 Simon B. Otto[1], Richard Servajean[2,3], Alexandre Lemopoulos[1], Anne-Florence Bitbol[2,3],
4 Melanie Blokesch[1*]
5
6 [1]Laboratory of Molecular Microbiology, Global Health Institute, School of Life
7 Sciences, École Polytechnique Fédérale de Lausanne (EPFL), CH-1015 Lausanne,
8 Switzerland
9 [2]Laboratory of Computational Biology and Theoretical Biophysics, Institute of
10 Bioengineering, School of Life Sciences, École Polytechnique Fédérale de Lausanne
11 (EPFL), CH-1015, Lausanne, Switzerland
12 [3]Swiss Institute of Bioinformatics, CH-1015 Lausanne, Switzerland
13
14 *Correspondence: melanie.blokesch@epfl.ch

bioRxiv preprint doi: https://doi.org/10.1101/2023.10.25.564063; this version posted October 26, 2023. The copyright holder for this preprint (which was not certified by peer review) is the author/funder, who has granted bioRxiv a license to display the preprint in perpetuity. It is made available under aCC-BY-ND 4.0 International license.

15 **Abstract**

16 The bacterial type VI secretion system (T6SS) is a widespread, kin-discriminatory
17 weapon capable of shaping microbial communities. Due to the system's dependency on
18 contact, cellular interactions can lead to either competition or kin protection. Cell-to-cell
19 contact is often accomplished via surface-exposed type IV pili (T4P). In *Vibrio*
20 *cholerae,* these T4P facilitate specific interactions when the bacteria colonize natural
21 chitinous surfaces. However, it has remained unclear whether and, if so, how these
22 interactions affect the bacterium's T6SS-mediated killing. In this study, we demonstrate
23 that pilus-mediated interactions can be harnessed to reduce the population of *V.*
24 *cholerae* under liquid growth conditions in a T6SS-dependent manner. We also show
25 that the naturally occurring diversity of pili determines the likelihood of cell-to-cell
26 contact and, consequently, the extent of T6SS-mediated competition. To determine the
27 factors that enable or hinder the T6SS's targeted reduction of competitors carrying pili,
28 we developed a physics-grounded computational model for autoaggregation.
29 Collectively, our research demonstrates that T4P involved in cell-to-cell contact can
30 impose a selective burden when *V. cholerae* encounters non-kin cells that possess an
31 active T6SS. Additionally, our study underscores the significance of T4P diversity in
32 protecting closely related individuals from T6SS attacks through autoaggregation and
33 spatial segregation.

34

35 Keywords: *Vibrio cholerae*; type VI secretion system; type IV pili; interbacterial
36 competition; agent-based model

bioRxiv preprint doi: https://doi.org/10.1101/2023.10.25.564063; this version posted October 26, 2023. The copyright holder for this preprint (which was not certified by peer review) is the author/funder, who has granted bioRxiv a license to display the preprint in perpetuity. It is made available under aCC-BY-ND 4.0 International license.

37 ## Introduction

38 The composition of microbial populations has a significant impact on ecological
39 functions and host health [1,2]. Interbacterial interactions are often antagonistic in
40 nature and target closely related species, ultimately influencing microbial populations
41 by aiding in niche colonization and exclusion [3–5]. In order to achieve this, bacteria
42 possess a myriad of weapons, and defence mechanisms [6]. Interactions between
43 species can be achieved through two primary mechanisms: the release of diffusible
44 compounds and contact-dependent interactions [7,8]. Unlike diffusible compounds,
45 which can disperse into the surrounding environment, contact-dependent mechanisms
46 require direct cell-to-cell interaction to effectively deliver toxins [9]. As a result,
47 contact-dependent mechanisms can precisely target neighbouring competitors without
48 the risk of toxin dilution in the surrounding liquid environment [10].

49 The Type VI secretion system (T6SS) is a widespread molecular apparatus that
50 relies on direct contact to inject toxic effector proteins into target cells [11]. It is
51 estimated to be found in more than 25% of gram-negative bacteria, encompassing both
52 environmental and pathogenic species [12]. The delivery of T6SS toxins has been
53 shown to influence microbial population compositions [13–15]. Importantly, the spatial
54 arrangement of competing cells also impacts the effectiveness of the T6SS [13,16].

55 The T6SS doesn't discriminate when targeting cells, owing to its indiscriminate
56 delivery method and toxins that disrupt widely conserved cellular processes [17]. To
57 prevent self-harm and protect kin, T6SS-positive bacteria produce matching pairs of
58 effector and immunity proteins [18]. Yet, bacteria can possess multiple T6SS gene
59 clusters along with variable auxiliary clusters that frequently encode additional effector
60 and immunity proteins [19]. Incompatibility in just one of these effector-immunity pairs
61 can drive T6SS competition [17,20]. Interestingly, targeted cells can also protect

bioRxiv preprint doi: https://doi.org/10.1101/2023.10.25.564063; this version posted October 26, 2023. The copyright holder for this preprint (which was not certified by peer review) is the author/funder, who has granted bioRxiv a license to display the preprint in perpetuity. It is made available under aCC-BY-ND 4.0 International license.

62 themselves through immunity-independent mechanisms, such as through the production
63 of extracellular polysaccharides and surface-attached capsules, allowing them to survive
64 T6SS attacks [21–23]. Furthermore, bacteria have been shown to withstand T6SS
65 challenge, and respond more potently [23–25].

66 Bacterial autoaggregation is a process that allows bacteria to bind to themselves,
67 often serving as a necessary step in forming biofilms [26,27]. This phenomenon is
68 frequently linked to pathogenicity as it provides protection against external threats, such
69 as phagocytosis [28] and antimicrobial agents [29,30]. Various molecules/structures,
70 often referred to as autoagglutinins, can facilitate this cell-to-cell binding [31]. Here, we
71 specifically focus on Type IV pili (T4P), which are common surface-exposed
72 appendages with diverse functions, including DNA uptake, motility, adhesion, and
73 aggregation [32,33]. T4P's ability to sense the environment is crucial for the survival,
74 colonization, and virulence of species carrying these pili [34]. For instance, the toxin
75 co-regulated pilus, exclusive to the pandemic lineage of *Vibrio cholerae*, plays a critical
76 role in host and interbacterial cell adhesion, which is vital for pathogenesis [35].
77 Similarly, T4P mediate interbacterial interactions in other pathogens like *Pseudomonas*
78 *aeruginosa* and *Neisseria meningitidis* [36,37]. However, this ability to sense the
79 environment and interact with other bacteria might inadvertently lead to unwanted cell-
80 to-cell contact, potentially inviting competition from the T6SS. It is therefore worth
81 noting that many autoagglutinins, including T4P, can modulate their level of
82 aggregation [31,38].

83 To explore the impact of the T6SS on bacterial behaviour in the context of T4P-
84 mediated cell-to-cell contact, we selected *V. cholerae* as our model organism. This
85 bacterium is notable for possessing both a T6SS and a variable DNA-uptake T4P.
86 Indeed, in *V. cholerae* strains, a single T6SS machinery is responsible for delivering

bioRxiv preprint doi: https://doi.org/10.1101/2023.10.25.564063; this version posted October 26, 2023. The copyright holder for this preprint (which was not certified by peer review) is the author/funder, who has granted bioRxiv a license to display the preprint in perpetuity. It is made available under aCC-BY-ND 4.0 International license.

87 distinct antibacterial effectors. These effectors are encoded within three genetic clusters,
88 including the primary large gene cluster that houses most of the structural components,
89 as well as auxiliary clusters 1 and 2 [19]. In some *V. cholerae* strains, including the
90 current pandemic lineage, there are additional auxiliary clusters that contain extra
91 effector-immunity pairs, although their presence varies [20,39–41]. It is worth noting
92 that in the aquatic environment, the presence of chitin degradation products has a dual
93 effect on *V. cholerae*: it activates both the T6SS machinery and the DNA-uptake T4P as
94 part of the bacterium's natural competence program. Consequently, T6SS-mediated
95 neighbour predation leads to DNA acquisition, ultimately driving horizontal gene
96 transfer through the process of natural transformation [42–44]. In the current pandemic
97 strains of *V. cholerae*, this activation is orchestrated by the TfoX master regulator once
98 the bacteria reach a high cell density state [42,43,45,46]. In environmental *V. cholerae*
99 isolates, the T6SS machinery is in a state of constant activity [20,47–50], representing
100 an immediate risk for T6SS-associated harm in case cell-to-cell contact in established.
101 Therefore, bacteria must distinguish between nearby individuals before intentionally
102 initiating cell-to-cell contact.

103 Prior research has shown that the DNA-uptake T4P, present in all *V. cholerae*
104 strains, often self-interacts and that it can distinguish between strains based on the
105 variability of the major pilin protein, PilA [51]. Interestingly, such variability in the
106 major pilin protein has been observed in various species carrying T4P [52–54]. Our
107 hypothesis therefore centres on the potential of T4P to be harnessed for targeted T6SS-
108 mediated bacterial elimination by facilitating specific cell-to-cell contact. Typically,
109 studies exploring T6SS-mediated killing are conducted on agar surfaces at high cell
110 densities, where physical contact is forced due to crowding. In contrast, T4P could
111 enable cell-to-cell contact with particular target cells under non-crowded (e.g., liquid)

bioRxiv preprint doi: https://doi.org/10.1101/2023.10.25.564063; this version posted October 26, 2023. The copyright holder for this preprint (which was not certified by peer review) is the author/funder, who has granted bioRxiv a license to display the preprint in perpetuity. It is made available under aCC-BY-ND 4.0 International license.

112 growth conditions, an idea that we tested in this study. We also sought to investigate the
113 relationship between the natural diversity of PilA and the T6SS, aiming to uncover the
114 strategies bacteria might employ to regulate the risk associated to establishing cell-to-
115 cell contact. Finally, we used simulations to determine the factors that might either
116 enable or impede the predation of T4P-carrying bacteria. Our simulations also
117 emphasize the critical role of spatial organization and rapid lysis in the success of
118 T6SS-mediated targeted depletion. Collectively, our study demonstrates that the natural
119 diversity of T4P plays a pivotal role in regulating the extent of non-kin cell-to-cell
120 contact, thus shaping the ensuing competition driven by the T6SS.
121

122 Results and discussion

123 T4P facilitate T6SS-mediated killing by fostering cell-to-cell contact.

124 We hypothesized that T4P-mediated autoaggregation might enhance the essential cell-
125 to-cell contact necessary for T6SS-mediated elimination under liquid conditions. To test
126 our hypothesis, we induced the activity of both T6SS and T4P by artificial induction of
127 the TfoX master regulator [43]. We then cocultured T6SS-competent strains (acting as
128 predator) with T6SS-sensitive target strains (prey). We made the prey strains T6SS-
129 sensitive by deleting the genes encoding the four T6SS effector/immunity protein pairs
130 (Δ4E/I), a modification applied to the pandemic *V. cholerae* strain A1552, which served
131 as the chassis for our research throughout this study. Predator strains were engineered to
132 be either T6SS-competent or rendered non-functional by deleting *vasK*, which encodes
133 a critical component of the T6SS membrane complex [55].

134 To investigate the role of T4P, we manipulated the major pilin PilA of A1552, a
135 pivotal T4P component. We either kept the encoding gene in its original genetic
136 location (*pilA*(A1552)) or deleted it (Δ*pilA*) in both the predator and prey strains. In all

bioRxiv preprint doi: https://doi.org/10.1101/2023.10.25.564063; this version posted October 26, 2023. The copyright holder for this preprint (which was not certified by peer review) is the author/funder, who has granted bioRxiv a license to display the preprint in perpetuity. It is made available under aCC-BY-ND 4.0 International license.

137 strains, we disabled T4P retraction (Δ*pilT*), which promoted an intensified
138 autoaggregation effect [51]. The phenomenon of amplified autoaggregation due to *pilT*
139 deletion has also been observed in other bacteria, such as *Neisseria meningitidis* [56]. In
140 this study, we employed *pilT* deletion as a practical approach to increase the likelihood
141 of self-interactions between pili. However, it's worth noting that these enhanced self-
142 interactions may resemble the interactions of T4P on chitin surfaces, where dense
143 networks of pili-pili interactions are well-documented [51]. Unfortunately, performing
144 experiments on chitin surfaces proved to be technically unfeasible for testing the
145 hypotheses outlined above.

146 Predator and prey strains were distinguishable by the presence of
147 antibiotic/fluorescent markers, which themselves displayed no discernible fitness
148 advantage or disadvantage when compared to a reference strain (Fig. S1A). We then
149 assessed the fitness of the predator strain over the prey strain by conducting bacterial
150 enumerations, followed by the calculation of the selection rate constant using the
151 method introduced by Travisano and Lenski [57]. Positive values of this constant
152 indicate a fitness advantage of the predator strain.

153 Our results clearly demonstrated a significant fitness advantage for the predator
154 strains when the T4P were functionally active (Fig. 1A). Conversely, when the predator
155 strain had a non-functional T6SS, any fitness advantage was entirely abolished. This
156 suggests that the fitness advantage observed in predator strains is primarily achieved
157 through T6SS-mediated depletion of prey cells.

158 To validate the T6SS-mediated depletion of prey cells, we conducted imaging of
159 the co-cultures, examining the spatial arrangement of prey and predator cells (Fig. 1B).
160 In order to image aggregates, cells were immobilised on an agarose pad and covered
161 with a coverslip (see method section for details). In our observations, we used a cell-

bioRxiv preprint doi: https://doi.org/10.1101/2023.10.25.564063; this version posted October 26, 2023. The copyright holder for this preprint (which was not certified by peer review) is the author/funder, who has granted bioRxiv a license to display the preprint in perpetuity. It is made available under aCC-BY-ND 4.0 International license.

162 impermeable DNA dye (SYTOX Blue) to visualise cells with compromised membrane
163 integrity [58]. What we observed was that the autoaggregation promoted by the T4P
164 effectively facilitated the necessary cell-to-cell contact for T6SS-mediated cell
165 elimination in liquid conditions. In contrast, the absence of functional T4P eliminated
166 the cell-to-cell contact, thereby preventing the killing of T6SS-sensitive strains.
167 Secondly, we noted cell rounding and lysis of T6SS-sensitive prey, a phenomenon
168 predominantly occurring in cells in direct contact with the predator strains (Fig. 1B,
169 inset). This particular trait was dependent on the presence of a T6SS-competent predator
170 strain, with no discernible changes in prey cell morphology when a non-functional
171 T6SS predator strain was utilized. Additionally, the phase contrast images revealed
172 larger aggregates, comprising multiple layers of cells, when a non-functional T6SS
173 predator strain was employed. Thus, these images offer compelling visual evidence of
174 T6SS-mediated prey cell elimination facilitated by the T4P.

175 To analyse the impact of the different interactions and parameters involved in
176 the T4P-facilitated T6SS-mediated depletion of prey strains, we developed an agent-
177 based model grounded in physical principles, incorporating key biological elements. In
178 this model, prey and predator bacteria were initially randomly distributed at a 1:1 ratio
179 in a three-dimensional $40 \times 40 \times 40$ body-centred cubic lattice modelling the liquid
180 suspension. Subsequently, all bacteria were allowed to move diffusively within the
181 medium, with the ability to divide and to interact through T4P. Predators could execute
182 T6SS-mediated killing of neighbouring prey cells, which then enter a lysing state (for
183 further details, refer to the methods section). By enabling or disabling interactions
184 through T4P and T6SS killing, we were able to qualitatively reproduce the microscopic
185 images observed (Fig. 1C). Just as in the experiments, when T4P were present, mixed
186 aggregates formed, leading to the lysis of prey cells when T6SS killing was enabled.

bioRxiv preprint doi: https://doi.org/10.1101/2023.10.25.564063; this version posted October 26, 2023. The copyright holder for this preprint (which was not certified by peer review) is the author/funder, who has granted bioRxiv a license to display the preprint in perpetuity. It is made available under aCC-BY-ND 4.0 International license.

187 Conversely, consistent with the experimental results, in the absence of T6SS killing,
188 larger aggregates were formed. Moreover, the absence of T4P prevented aggregation,
189 with T6SS killing becoming a rare event. Therefore, our minimal model serves to
190 confirm that prey depletion is significantly enhanced when predator and prey cells
191 adhere via T4P. This heightened contact between neighbouring prey-predator pairs
192 allows for more frequent T6SS killing. Additionally, in the presence of T4P without
193 T6SS killing, bacteria formed mixed aggregates, with a minor tendency to develop
194 homogeneous patches due to cell division. This outcome aligns with the experimental
195 observations, where a low level of patchiness was consistently noted.

196 In light of these observations, we were keen to delve into the dynamics of
197 contact establishment and the subsequent elimination of prey. To investigate this, we
198 conducted a time-course co-culture experiment in which we determined the selection
199 rate of the predator strain at different incubation times (Fig. 1D). Furthermore, we
200 assessed the levels of aggregation in these co-cultures by comparing the ratio of cells in
201 the solution to those in the settled aggregates (Fig. 1E). What we found was that the
202 fitness advantage of predator strains became evident when compared to a Δ*pilA* co-
203 culture control after 3.5-4 hours of incubation. This synchronization with a preceding
204 rapid aggregation event suggests that the killing of T6SS-sensitive cells occurs shortly
205 after cell-to-cell contact is established. Similar to the experimental observations,
206 simulations exhibit rapid aggregation, followed by T6SS killing (Fig. S2, Movie S1-4).
207 Collectively, our data demonstrate that T4P-mediated aggregation generates enough
208 cell-to-cell contact to facilitate effective T6SS killing, even under conditions where
209 cells are otherwise well-mixed.

210 Related to this role of T4P in facilitating T6SS-mediated killing in liquid
211 environments, studies have demonstrated that engineered receptor-ligand interactions

bioRxiv preprint doi: https://doi.org/10.1101/2023.10.25.564063; this version posted October 26, 2023. The copyright holder for this preprint (which was not certified by peer review) is the author/funder, who has granted bioRxiv a license to display the preprint in perpetuity. It is made available under aCC-BY-ND 4.0 International license.

212 can lead to the targeted depletion of prey cells within bacterial communities [59].
213 Similarly, in *Vibrio fischeri*, a putative lipoprotein has been implicated in mediating
214 targeted cell-to-cell contact for T6SS competition in high-viscosity liquid media [10].
215 It's worth noting that this lipoprotein's distribution is limited to bacterial species
216 associated with a marine host and has no homolog in *V. cholerae*. The specificity of
217 target recognition in this case is achieved through an unknown ligand. In various
218 scenarios, not limited to liquid conditions, such as within microcolonies of *Neisseria*
219 *cinerea*, the expression of T4P by both predator and prey strains heightened the prey's
220 vulnerability to T6SS attacks in contrast to a non-piliated control. This effect was
221 achieved by preventing the segregation of prey from a T6SS-armed attacker [60]. These
222 findings underscore the potential risk involved in utilizing T4P, as they can serve as
223 potential enhancer of T6SS-mediated competition.
224

225 **Naturally occurring diversity of T6SS E/I pairs and T4P pilin alleles.**

226 Having demonstrated the potential of T4P to facilitate T6SS-mediated killing in liquid
227 environments, our next objective was to investigate the interplay between the naturally
228 occurring diversity of T6SS and T4P in *V. cholerae*. We were interested in
229 understanding whether there was a selection pressure leading to coevolution between
230 the *pilA* alleles and T6SS compatibility, or if other selective forces influenced the
231 diversity of these two systems. To address this question, we initially constructed a
232 cladogram involving 39 *V. cholerae* genomes, comprising both environmental and
233 patient isolates. We used *Vibrio mimicus* as an outgroup for this analysis (Fig. 2A). To
234 evaluate the diversity of the T6SS, we aligned the nucleotide sequences of the six
235 known T6SS clusters. We then extracted the amino acid sequences of the core immunity
236 proteins. The resulting heatmaps, displaying the percentage identity of T6SS (Figs. S3-

bioRxiv preprint doi: https://doi.org/10.1101/2023.10.25.564063; this version posted October 26, 2023. The copyright holder for this preprint (which was not certified by peer review) is the author/funder, who has granted bioRxiv a license to display the preprint in perpetuity. It is made available under aCC-BY-ND 4.0 International license.

237 S8), were used to group T6SS effector/immunity (E/I) modules into families (sharing
238 over 30% identity) and subfamilies (identical sequences) consistent with methods
239 previously developed [17,61]. This typing approach enabled us to identify six novel
240 T6SS effector/immunity families within the large gene cluster. Additionally, it
241 expanded our understanding of strains carrying the recently discovered auxiliary
242 clusters 4 and 5 [20,40,41] (Fig. 2A).

243 The categorization of strains into T6SS families, as depicted to the right of the
244 cladogram in Figure 2A, allowed us to visualize whether they are capable of coexisting,
245 sharing identical T6SS modules, or if they can engage in T6SS-dependent competition.
246 Variety in T6SS families within *V. cholerae* isolates was large, with few T6SS
247 compatible strains. Indeed, previous experimental data among a subset of strains
248 showed limited compatibility between non-kin T6SS systems [20]. Next, we examined
249 the experimentally confirmed self-interaction ability of PilA, which is presented
250 alongside the T6SS modules. We also extracted nucleotide and protein sequences based
251 on genome annotations to construct a heatmap and a PilA cladogram (Fig. S9-10).
252 Notably, the studied PilA variants exhibit high variability and cluster into numerous
253 phylogenetic groups.

254 Our analysis did not reveal distinct clades for either the T6SS E/I modules or PilA
255 variants (Fig. 2A, S10). While closely related strains occasionally shared similar T6SS
256 E/I modules and PilA variants (for example, strains Env9 and Env390), more often, we
257 observed diversity in both the T6SS E/I modules and PilA variants (such as SP7G and
258 DL4215). Indeed, we did not identify clear-cut markers of coevolution between PilA
259 variants and T6SS compatibility. Furthermore, we observed a lack of congruence
260 between genome-based and *pilA* topologies (Fig. S10) and an average approximately
261 9% lower GC content for both the T6SS E/I modules and *pilA*. These observations

bioRxiv preprint doi: https://doi.org/10.1101/2023.10.25.564063; this version posted October 26, 2023. The copyright holder for this preprint (which was not certified by peer review) is the author/funder, who has granted bioRxiv a license to display the preprint in perpetuity. It is made available under aCC-BY-ND 4.0 International license.

262 suggest that both *pilA* and T6SS E/I modules can be horizontally acquired, as previously
263 suggested for the latter [17,62]. Horizontal exchange of *pilA* alleles or T6SS E/I
264 modules could thereby alter bacterial competition, as outlined below.
265
266 **T4P-facilitated neighbour predation is conserved among self-interacting PilA**
267 **variants.**
268 Subsequently, we assessed whether the capacity of T4P to facilitate T6SS-mediated
269 killing is conserved among different PilA variants. To investigate PilA variability, we
270 introduced *pilA* alleles into the native *pilA* locus of strain A1552, a method previously
271 demonstrated to be fully functional [51]. The predator and prey strains with replaced
272 *pilA* (*pilA*rep) were co-cultured, and their predator selection rates were evaluated (Fig.
273 2B,C). Our results revealed a positive predator selection rate for PilA variants capable
274 of self-interaction, as compared to a negative control lacking *pilA* (Δ*pilA*; Fig. 2B).
275 Conversely, PilA variants that could not self-interact according to previous work [51]
276 were unable to facilitate T6SS-mediated killing (Fig. 2C).
277 Interestingly, two PilA variants, from strains SL6Y and DRC186, displayed an
278 intermediate level of prey strain depletion. Both of these PilA variants could support the
279 killing of T6SS-sensitive prey, but the culture tubes appeared more turbid than those
280 with other self-interacting PilA variants that mostly settled to the bottom of the tube.
281 We hypothesized that a weaker aggregation phenotype might allow a subpopulation of
282 targeted prey cells to escape. To explore this, we determined the aggregation levels of
283 these PilA variants and compared them to the strongly self-interacting A1552 PilA
284 variant and the negative Δ*pilA* control (Fig. 2D). While measuring aggregation ratios
285 [51], various settling times were considered to allow for self-interaction of potentially
286 weaker PilA variants. Indeed, both the SL6Y and DRC186 PilA variants exhibited

bioRxiv preprint doi: https://doi.org/10.1101/2023.10.25.564063; this version posted October 26, 2023. The copyright holder for this preprint (which was not certified by peer review) is the author/funder, who has granted bioRxiv a license to display the preprint in perpetuity. It is made available under aCC-BY-ND 4.0 International license.

287 weaker levels of aggregation than the strongly self-interacting A1552 PilA variant. Of
288 these two, the SL6Y variant displayed stronger aggregation during extended settling
289 periods, which are, however, not included in the evaluation of the predator selection rate
290 during co-culture. The major pilin of T4P often exhibits variation [52–54]. This
291 variability can influence the strength of attractive forces between bacterial cells, which
292 can explain our results. Such an effect was seen in *Neisseria gonorrhoeae* [63].
293 Similarly, the diversity in PilA variants in *Acinetobacter baumannii* was shown to
294 impact the level of T4P self-interaction and its functional specialization [54].
295
296 **Pilus-specific T6SS competition by spatial segregation.**
297 A significant diversity of PilA variants is naturally present within the non-pandemic *V.*
298 *cholerae* isolates. We speculated that PilA diversity might provide protection for cells
299 against T6SS competition by enabling specificity in contact establishment. To
300 investigate this, we conducted a co-culture experiment in which we co-cultivated a prey
301 strain with various PilA variants alongside a predator strain containing the pandemic
302 A1552 PilA variant (Fig. 3A). As expected, the presence of PilA diversity negated the
303 fitness advantage of the predator strain, in contrast to the co-culture with a control T4P
304 matching the A1552 PilA variant.
305 After this discovery, we proceeded to visualize the spatial arrangement of the
306 cells, both with and without PilA diversity (Figs. 3B, S11). While identical T4P led to a
307 well-blended community with numerous interfaces of cell-to-cell contact between the
308 two cell types, T4P diversity facilitated the predominant spatial separation of the two
309 cell types. Consequently, due to the T4P specificity between the pandemic and other
310 self-interacting PilA variants, T4P-mediated T6SS competition with strains carrying
311 diverse *pilA* alleles was circumvented. We therefore conducted simulations that

bioRxiv preprint doi: https://doi.org/10.1101/2023.10.25.564063; this version posted October 26, 2023. The copyright holder for this preprint (which was not certified by peer review) is the author/funder, who has granted bioRxiv a license to display the preprint in perpetuity. It is made available under aCC-BY-ND 4.0 International license.

312 accounted for the presence of non-matching T4P incapable of cross-interaction, in
313 contrast to matching T4P (Fig. 3C, Movie S4-5). Similar to the experimental
314 observations, prey and predator cells with diverse T4P formed distinct aggregates. This
315 prevented encounters between the prey and predator, along with subsequent T6SS-
316 mediated killings, within the timescale considered.

317 Most PilA variants of *V. cholerae* appear to exhibit highly specific interactions
318 [51]. Interestingly, naturally occurring PilA variants with cross-interaction have also
319 been identified. These promiscuous PilA variants could facilitate cell-to-cell contact
320 between potential T6SS competitors and invite T6SS competition. We hypothesized that
321 the potential fitness disadvantage of T6SS competition could be offset by preferential
322 binding to kin. To further investigate this, we simulated prey and predator interactions,
323 in which we reduced the cross-interaction T4P binding energy (E_{cross}) between prey
324 and predator, making cross-interaction weaker than self-interaction (Fig. 3D, Movie
325 S6). These simulations resulted in patchy aggregates. Increasing E_{cross} within this range
326 led to increased mixing within aggregates, providing more boundary interfaces between
327 prey and predator, until the cross-interaction T4P binding energy equalled the self-
328 interaction T4P binding energy between two prey cells or two predators, resulting in an
329 aggregate simulating matching T4P. Simulating preferential binding to kin restricted
330 T6SS killing predominantly to the boundary interfaces between patches, thanks to the
331 partial segregation effect arising from weaker interactions across T4P variants.

332 Next, we performed coculture experiments to evaluate the predator selection rate
333 of all known promiscuous interactions, as well as their conforming counterparts (Fig.
334 3E). Simultaneously, we determined the spatial organization of the cells for all
335 promiscuous interactions (Figs. 3F, S12). Compared to the matching A1552 PilA
336 variant condition, we observed two distinct phenotypes. The promiscuity between

bioRxiv preprint doi: https://doi.org/10.1101/2023.10.25.564063; this version posted October 26, 2023. The copyright holder for this preprint (which was not certified by peer review) is the author/funder, who has granted bioRxiv a license to display the preprint in perpetuity. It is made available under aCC-BY-ND 4.0 International license.

337 SA3G and SP6G PilA variants resulted in low-level mixing, with sparse non-kin cell-to-
338 cell contact at boundary interfaces. This led to no fitness advantages for T6SS
339 competent cells at the population level, as evident from the determined predator
340 selection rate. For the other promiscuous PilA variant combinations, we observed an
341 intermediate phenotype. Segregated groups of cell types were observed, leading to a
342 subpopulation of cells engaging in non-kin cell-to-cell contact, while others established
343 cell-to-cell contact between kin cells. This matches the predictions from our model,
344 since the simulations that modelled preferential binding to kin produced aggregates of
345 similar morphology to both types of promiscuous T4P, depending on the exact value of
346 the cross-interaction T4P binding energy (E_{cross}). This suggests that weaker
347 interactions between promiscuous T4P variants are responsible for the observed spatial
348 organization patterns. The resulting patchiness leads to a reduction of T6SS competition
349 interfaces compared to the case with matching pili, and subdivides the potential fitness
350 advantages or disadvantages of T6SS competition to a subset of the population,
351 resembling a bet-hedging strategy. Alternatively, intrinsically modulating the strength
352 or ability of T4P to self-interact (e.g. SL6Y/SA5Y) would reduce the number of all
353 T4P-facilitated cell-to-cell contacts but may affect the functional specialization of the
354 strain. Lastly, the predominant PilA variant specificity found in naturally occurring
355 isolates suggests a selective burden for ambiguous T4P. Although we demonstrate that
356 T6SS competition could apply a selective burden for pilus conformity, we suggest that
357 diversity in both T6SS and PilA is also driven by factors independent of their interplay.
358 Namely, T4P-independent T6SS competition, potentially caused through proximity by
359 crowding, could also drive the diversity observed in T6SS E/I modules, while the PilA
360 variability might reflect the selection pressure by other stressors, such as phage
361 predation.

bioRxiv preprint doi: https://doi.org/10.1101/2023.10.25.564063; this version posted October 26, 2023. The copyright holder for this preprint (which was not certified by peer review) is the author/funder, who has granted bioRxiv a license to display the preprint in perpetuity. It is made available under aCC-BY-ND 4.0 International license.

362

363 **Spatial assortment and lysis time dictate T6SS-mediated target cell depletion.**

364 With evidence of T4P's potential in facilitating T6SS depletion, we aimed to explore the
365 key factors influencing its effectiveness using our agent-based model. Considering the
366 observed ability of T4P to regulate non-kin cell-to-cell contact, we assessed the impact
367 of cross-interaction T4P binding energy on mixing levels (Fig. 4A). To quantitatively
368 analyse the mixing within aggregates, we evaluated assortment, which compares the
369 number of observed adjacent prey-predator pairs to its maximum expected value in the
370 case of random mixing (see methods). Similar to the experimental observations, our
371 simulations demonstrate that a non-zero cross-interaction T4P binding energy (E_{cross})
372 between prey and predator increases assortment, thereby promoting mixing. Higher
373 cross-interaction T4P binding energy between prey and predator results in the formation
374 of more mixed aggregates, with larger E_{cross} values leading to increased spatial
375 assortment. Moreover, we noted a stronger long-term gradual rise in assortment over
376 time in the presence of T6SS killing compared to scenarios without T6SS killing. The
377 action of T6SS results in the lysis of prey cells that do not undergo division, thus
378 reducing the division-induced tendency of aggregates to develop distinct patches. Under
379 infinite time, all T6SS killing simulations would eventually become uniform, consisting
380 solely of predators, corresponding to fixation of the predator type. However, it is crucial
381 to highlight that our simulations do not account for the potential escape of divided prey
382 cells into new niches. In natural settings, the observed delay in spatial assortment for
383 lower values of E_{cross} could potentially be exploited by the T6SS-sensitive prey.

384 Having quantified how T4P cross-interactions shape spatial assortment, we
385 aimed to determine the impact of these interactions on the predator selection rate (Fig.
386 4B). We observed a rapid increase in the selection rate with time, greatly influenced by

bioRxiv preprint doi: https://doi.org/10.1101/2023.10.25.564063; this version posted October 26, 2023. The copyright holder for this preprint (which was not certified by peer review) is the author/funder, who has granted bioRxiv a license to display the preprint in perpetuity. It is made available under aCC-BY-ND 4.0 International license.

387 the value of the prey-predator T4P binding energy. When $E_{cross} = 0$, this increase was
388 minimal within the time scale considered. Therefore, strong T4P-mediated attraction
389 between prey and predator plays a crucial role in promoting T6SS competition, a
390 condition achieved by matching T4P, and modulated by promiscuous T4P. We observed
391 a positive relationship between the predator selection rate and E_{cross}, with T6SS
392 competition being enhanced as prey-predator attraction increases towards ambiguity
393 (Fig. 4C). Matching T4P would ensure a strong binding energy between cell types,
394 leading to the subsequent T6SS depletion of target strains, while diverse T4P would
395 hinder T6SS competition, depending on the level of promiscuity of the PilA variant.
396 Through PilA diversity, spatial assortment is modulated, dictating the dynamics of
397 T6SS-mediated depletion of target strains by altering the level of T6SS competition
398 interfaces. Indeed, autoaggregation facilitated by self-interacting identical T4P could
399 function as a defence strategy of *V. cholerae* against T6SS invaders.

400 Interestingly, the reduction in T6SS competition interfaces observed in the
401 simulations and imaging of promiscuous T4P resulted in lysing cells forming a barrier
402 between cell types. This phenomenon, known as the corpse barrier effect [64], could
403 significantly influence the dynamics of prey depletion. To further investigate this, we
404 determined the predator selection rate with various lysis times (Fig. 4D) [65]. We
405 observed a negative relationship between lysis time and predator selection rate.
406 Consistent with the findings of Smith and colleagues [64], the corpse barrier effect
407 impedes T6SS competition by obstructing predators from reaching new targets. Predator
408 cells equipped with fast-acting lysing effector modules could overcome this barrier,
409 which might be a critical factor in considering target depletion. In *V. cholerae*, strain
410 W10G, carrying two pandemic-like A-type E/I modules in the large and aux2 clusters,
411 has been shown to exhibit strong killing activity against other environmental *V.*

bioRxiv preprint doi: https://doi.org/10.1101/2023.10.25.564063; this version posted October 26, 2023. The copyright holder for this preprint (which was not certified by peer review) is the author/funder, who has granted bioRxiv a license to display the preprint in perpetuity. It is made available under aCC-BY-ND 4.0 International license.

412 *cholerae* strains [20]. Moreover, *Vibrio coralliilyticus*, while not resistant to *V. cholerae*
413 T6SS attacks, can withstand T6SS challenge and deplete pandemic *V. cholerae* through
414 T6SS killing [25]. Lastly, spatial assortment could prevent the formation of a corpse
415 barrier, as demonstrated in our experiments. Mixing between predator and prey cells,
416 promoted by matching T4P, increases T6SS competition interfaces. However, it remains
417 to be investigated whether this mixing occurs under host or environmental conditions.

418 Thus, an important question for future research will be to comprehend whether
419 under natural conditions, T4P could serve as a means for the recruitment of predator
420 cells. This exploration could also yield further insights into the consequences of T6SS
421 and T4P on the local enrichment of pathogenic or environmental strains, as well as PilA
422 variant specialization for *V. cholerae*, specifically. Nonetheless, the swift capture and
423 subsequent elimination of pandemic *V. cholerae* through pilus conformity observed in
424 our experiments have demonstrated the potential for the targeted depletion of T4P-
425 carrying species.

426 The critical role of self-interacting T4P in the colonization of pathogen hosts and
427 environmental niches may contribute to the maintenance of the targeted receptor. For
428 instance, in *V. cholerae*, the conservation of the strongly self-interacting PilA variant
429 within the pandemic lineage suggests its significance in the aquatic environment and/or
430 during human transmission [51]. Additionally, the preservation of T4P specificity might
431 prevent T4P-facilitated competition with T6SS-carrying competitors. In contrast, the
432 self-interacting toxin co-regulated pilus, exclusive to the *V. cholerae* pandemic lineage,
433 does not display target specificity between major pilin variants [51,66]. It is important
434 to note that the T6SS E/I modules of pandemic strains are identical, rendering them
435 T6SS compatible. Finally, considering the natural occurrence of diverse self-interacting

bioRxiv preprint doi: https://doi.org/10.1101/2023.10.25.564063; this version posted October 26, 2023. The copyright holder for this preprint (which was not certified by peer review) is the author/funder, who has granted bioRxiv a license to display the preprint in perpetuity. It is made available under aCC-BY-ND 4.0 International license.

436 T4P in various pathogens [31,53,54,67], the investigation of targeted depletion using
437 T4P should be pursued further.
438

439 ## Materials and methods

440 **Bacterial strains and growth conditions.**

441 The bacterial strains and plasmids used in this study are listed in Supplementary Table
442 1. O1 El Tor strain A1552 was used as a genome-sequenced representative of the
443 ongoing seventh cholera pandemic [68,69]. Unless otherwise specified, bacteria were
444 cultured in lysogeny broth (LB) (Carl Roth, Switzerland) or on LB agar plates. The LB
445 medium was supplemented with 1 mM $CaCl_2$ and 5 mM $MgCl_2$ to counteract LB batch-
446 to-batch variability in aggregation [51]. Indeed, LB medium is often low in divalent
447 cations [70], and $CaCl_2$ and $MgCl_2$ concentration can be vastly different between
448 batches/different producers [71]. Notably, the $CaCl_2$ and $MgCl_2$ concentrations present
449 in seawater are, on average, considerably higher than those supplemented in this study
450 [72]. Despite this, the addition of divalent cations has been found to have no effect on
451 T6SS secretion, although it has been observed to impact the conditional efficacy of
452 certain T6SS effectors [71,73].

453 Cultures were induced with 0.2% L-arabinose to promote the expression of
454 P_{BAD}-driven genes that were carried by a mini-Tn7 transposon [74] integrated on the
455 chromosome. Post-bacterial mating, *Escherichia coli* cells were counter-selected using
456 Thiosulfate citrate bile salts sucrose (TCBS, Sigma-Aldrich) agar. SacB-based counter-
457 selection was carried out on NaCl-free LB agar supplemented with 10% sucrose.
458 Various antibiotics such as ampicillin (Amp, 100 μg ml^{-1}), gentamicin (Gent, 50 μg
459 ml^{-1}), kanamycin (Kan, 75 μg ml–1), or spectinomycin (Spec, 200 μg ml^{-1}) were added
460 when necessary. Prior to each experiment, overnight cultures were adjusted to an optical

bioRxiv preprint doi: https://doi.org/10.1101/2023.10.25.564063; this version posted October 26, 2023. The copyright holder for this preprint (which was not certified by peer review) is the author/funder, who has granted bioRxiv a license to display the preprint in perpetuity. It is made available under aCC-BY-ND 4.0 International license.

461 density at 600nm (OD_{600}) of 2.0 and if required, mixed in a 1:1 ratio, before being back-
462 diluted 1:100 in fresh LB medium. These cultures were incubated in 14 ml round-
463 bottomed polystyrene test tubes (Falcon, Corning) on a carousel style rotary wheel (40
464 rpm) at 30°C.
465
466 **Bacterial strain engineering.**
467 Standard methods were used for DNA manipulations and molecular cloning [75]. All
468 genetically engineered strains were verified by PCR, Sanger sequenced by Microsynth
469 AG and analysed using SnapGene (v. 4.3.11). Genetic engineering of *V. cholerae* was
470 done by natural transformation followed by FLP recombination (TransFLP) [76–78],
471 tri-parental mating [79] or allelic exchange using the counter-selectable plasmid
472 pGP704-Sac28 [80].
473
474 **Bacterial competition assays.**
475 The selection rate of predator strains was evaluated in co-culture experiments using the
476 specified predator-prey strain pairs. Cultures were typically grown for 6 h, followed by
477 a wash step in PBS and subsequent vortexing for 10 min at maximum speed to disperse
478 the aggregates into single cells. Right after dispersion, cells were serially diluted in
479 PBS, and both prey and predator strains were counted on selective antibiotic-containing
480 plates.
481 The selection rate of the predator was calculated as the difference in the
482 Malthusian parameters of both strains:
483 $r = \ln[N_{predator}(t = 1)/N_{predator}(t = 0)] - \ln[N_{prey}(t = 1)/N_{prey}(t = 0)]$, where
484 $t = 1$ is the numerical density (N) at the end of the experiment [57].

bioRxiv preprint doi: https://doi.org/10.1101/2023.10.25.564063; this version posted October 26, 2023. The copyright holder for this preprint (which was not certified by peer review) is the author/funder, who has granted bioRxiv a license to display the preprint in perpetuity. It is made available under aCC-BY-ND 4.0 International license.

485 The relative fitness of the strains carrying antibiotic/fluorescent markers was
486 determined in co-culture experiments using A1552Δ*lacZ* as the reference strain,
487 following previously established methods [81]. Overnight cultures were prepared as
488 described earlier, but back-diluted to an OD_{600} of approximately 0.0016 in fresh LB
489 medium and grown without antibiotics for 8 h. At the beginning and end of the
490 experiment, the proportions of blue (tested strain) and white (reference strain) colonies
491 were counted through serial dilution in PBS, followed by plating on LB agar plates
492 supplemented with 5-bromo-4-chloro-3-indolyl β-d-galactopyranoside (X-gal; 40 μg
493 ml^{-1}).

494 The relative fitness was calculated as the ratio of the Malthusian parameters of
495 blue over white colonies: $W = \ln[N_{blue}(t = 1)/N_{blue}(t = 0)] / \ln[N_{white}(t =$
496 $1)/N_{white}(t = 0)]$, where $t = 1$ is the numerical density (N) at the end of the
497 experiment [82].

498

499 **Bacterial imaging through light microscopy.**

500 To visualise aggregates, overnight cultures were back-diluted, as mentioned previously,
501 and were grown for 4 h. The cells were immobilized by mounting them on slides coated
502 with an agarose pad (1.2% wt/vol in PBS), covered with a coverslip, and imaged using a
503 Zeiss Axio Imager M2 epifluorescence microscope with an AxioCam MRm camera,
504 controlled by Zeiss Zen software (ZEN 2.6 blue edition). Images were captured using a
505 Plan-Apochromat ×100/1.4-NA Ph3 oil objective illuminated by an HXP120 lamp and
506 were analysed and prepared for publication using Fiji [83]. To stain lysed cells, the
507 agarose pad was supplemented with 0.5 μM SYTOX Blue Nucleic Acid Stain (Thermo
508 Fisher Scientific) as previously described [58].

509

bioRxiv preprint doi: https://doi.org/10.1101/2023.10.25.564063; this version posted October 26, 2023. The copyright holder for this preprint (which was not certified by peer review) is the author/funder, who has granted bioRxiv a license to display the preprint in perpetuity. It is made available under aCC-BY-ND 4.0 International license.

510 **Bacterial aggregation assay.**

511 Aggregation assays were conducted following the established protocol [51]. Bacteria
512 were grown for 6 h, and unless specified allowed to settle for 30 minutes, or 5 minutes
513 for the time-course experiment (Fig. 1E). The level of aggregation was determined by
514 measuring the OD_{600} before and after vortexing (vortexed at maximum speed for
515 approximately 5 sec), during which the settled aggregates were resuspended into the
516 solution.

517

518 **Computational model development and testing**

519 An agent-based model was developed on a lattice, grounded in physical principles and
520 incorporating the key biological components of the system. The focus was directed
521 towards the events subsequent to the induction of T4P and T6SS, precisely from the 3-
522 hour mark in the experiments. Stochastic simulations of the model were conducted,
523 employing experimentally measured parameter values whenever available. The model
524 was simulated on a lattice in both two and three dimensions (Fig. S13), with primary
525 emphasis placed on the three-dimensional case in the main text, owing to its closer
526 approximation to real-world conditions. In the three-dimensional case, each cell sits on
527 a site of a body-centred cubic lattice. The following section outlines the fundamental
528 components of the model.

529

530 *Division*

531 In our model, a cell can divide with rate k_{div}, matching the experimentally measured
532 value, if at least one of its neighbouring sites on the lattice is empty. The offspring is
533 identical to its parent cell and is placed on a randomly chosen empty neighbouring site.
534 In our experiments, the cell division rate was determined to be $k_{div} = 1.58h^{-1}$. The

bioRxiv preprint doi: https://doi.org/10.1101/2023.10.25.564063; this version posted October 26, 2023. The copyright holder for this preprint (which was not certified by peer review) is the author/funder, who has granted bioRxiv a license to display the preprint in perpetuity. It is made available under aCC-BY-ND 4.0 International license.

535 growth rate was calculated using the formula $k_{div} = \ln[(OD_2/OD_1)/(T_2 - T_1)]$, where
536 OD represents the optical density and T represents the incubation time. The values 1
537 and 2 correspond to the start and end, respectively, of the linear portion of the optical
538 density curve of the wild-type *V. cholerae* grown under the specified growth conditions.
539 Exact measurements can be found in the source data file.

540

541 *Transport*

542 In our experimental setup, the bacteria are placed in test tubes and subjected to agitation
543 through rotation. This is relevant due to the turbulent flow observed in the natural
544 habitat of *V. cholerae*, predominantly in oceans, estuaries, and rivers [84–86]. In such a
545 turbulent regime, passive transport by the medium can be modelled by eddy diffusion.
546 In addition, *V. cholerae* bacteria can actively swim, but the agitation of the medium
547 prevents any substantial gradient that might bias their motion via chemotaxis or quorum
548 sensing. Thus, their active swimming motion may also be simply modelled by diffusion
549 [87]. We therefore model transport through an effective diffusion coefficient D, which
550 incorporates both passive and active transport.

551 Eddy diffusion coefficients are challenging to measure as they are contingent on
552 local flow velocity and the sizes of eddies [86]. However, they are usually significantly
553 larger than the molecular diffusion coefficient $D_{mol} = 5\times10^{-13} m^2{\cdot}s^{-1}$, obtained via
554 the Stokes-Einstein equation $D_{mol} = kT/\,(6\pi\eta R)$, where k is the Boltzmann constant,
555 $T = 300\,K$ is the absolute temperature, $\eta = 8\times10^{-4} Pa.s$ denotes the dynamic viscosity
556 of water and R is the effective radius of bacteria, i.e. the radius of a sphere with the
557 experimentally-measured volume of a wildtype *V. cholerae* bacterium [88]. Active
558 diffusion coefficients associated to swimming can be expressed from the properties of
559 bacterial swimming trajectories [87], and are of the order of $10^{-11} m^2{\cdot}s^{-1}$ for

bioRxiv preprint doi: https://doi.org/10.1101/2023.10.25.564063; this version posted October 26, 2023. The copyright holder for this preprint (which was not certified by peer review) is the author/funder, who has granted bioRxiv a license to display the preprint in perpetuity. It is made available under aCC-BY-ND 4.0 International license.

560 *Escherichia coli* run and tumble motion. In our simulations, we adopted a
561 phenomenological value of $D = 3{\times}10^{-12} m^2{\cdot}s^{-1}$, which was found to reproduce the
562 experimentally observed aggregate formation in the absence of killing by T6SS.
563 However, we note that there is uncertainty on this value. For instance, *V. cholerae* was
564 recently found to swim faster than *E. coli* [89], which could yield a larger effective
565 diffusion coefficient. An increased diffusion coefficient should mainly accelerate cluster
566 formation – and would make simulations more computationally demanding.
567 Importantly, previous work had shown that aggregate formation is maintained in non-
568 motile *V. cholerae* [51].

569 In addition to individual bacterial cells, aggregates of bacteria bound by T4P
570 interactions may also diffuse as a single unit. We include this effect for completeness,
571 but it is worth noting that there are various possible detailed choices for its
572 implementation (Are neighbouring non-bound bacteria pushed by a moving aggregate?
573 Are they pulled by it? Can aggregates break into large blocks? Can they merge? Is their
574 effective diffusion coefficient the same as for single bacteria? For simplicity we
575 answered yes, no, no, yes and yes to these questions). Given these complications,
576 simulations were also conducted without considering any aggregate diffusion. Figure
577 S14 demonstrates that simulations with and without aggregate diffusion exhibit the
578 same phenomenology in the case of diverse T4P, and we also obtained similar results in
579 other cases. Therefore, this effect or its variants do not influence our conclusions.

580 In practice, in our lattice model, diffusion is implemented via bacteria hopping
581 randomly to any free neighbouring site, with a rate k_{hop} which is derived from the
582 diffusion coefficient: $k_{hop} = dD/(2zR^2)$, where $d = 3$ is the dimension considered
583 (3D here), $z = 8$ is the number of nearest neighbours per site in the body-centred cubic
584 lattice, and R is the effective radius of a bacteria (see above). Since each site has 8

bioRxiv preprint doi: https://doi.org/10.1101/2023.10.25.564063; this version posted October 26, 2023. The copyright holder for this preprint (which was not certified by peer review) is the author/funder, who has granted bioRxiv a license to display the preprint in perpetuity. It is made available under aCC-BY-ND 4.0 International license.

585 neighbours, the total hopping rate of a bacteria is $8k_{hop}$, if all its neighbouring sites are
586 free.
587
588 *Interactions via T4P*
589 The effect of T4P is modelled as an attractive interaction between neighbouring bacteria
590 on the lattice. Considering that the T4P of prey and predators may differ, three types of
591 interactions are considered, each with potentially different binding energies: E_{prey}
592 between two prey cells, $E_{predator}$ between two predators and E_{cross} between a prey and
593 a predator. Importantly, these interactions have an impact on the ability of individual
594 bacteria to diffuse. Qualitatively, a bacterium bound to many others will be less likely to
595 move away, due to the requirement of detaching from its neighbours. To model this, we
596 assume a dynamics that ensures detailed balance for these moves [90]. The hopping rate
597 of a prey to any free neighbouring site is $nk_{hop}\exp(-n_{prey}E_{prey} - n_{predator}E_{cross})$
598 where k_{hop} is the baseline hopping rate of a freely diffusing bacterium, while n is the
599 number of free neighbouring sites, n_{prey} the number of neighbouring prey and
600 $n_{predator}$ the number of neighbouring predators. A similar formula can be written for a
601 predator.
602 We are not aware of precise measurements of the binding energy associated with
603 T4P in *V. cholerae*. However, the involved interactions are reversible protein-protein
604 interactions, and thus, we expect them to be on the order of a few kT, where kT is the
605 scale of thermal fluctuations (k being the Boltzmann constant and T the absolute
606 temperature). Because T4P binding energies are not precisely known, we varied them in
607 our simulations [91]. The first key point is that they need to be strong enough to ensure
608 effective aggregation of prey and predator separately, as observed in the experiments.
609 Indeed, as shown in Figure S15, in a system where there is only this attraction and

bioRxiv preprint doi: https://doi.org/10.1101/2023.10.25.564063; this version posted October 26, 2023. The copyright holder for this preprint (which was not certified by peer review) is the author/funder, who has granted bioRxiv a license to display the preprint in perpetuity. It is made available under aCC-BY-ND 4.0 International license.

610 transport (no division, no killing), aggregation occurs above $2kT$ in 2D and $2.5kT$ in
611 3D at the densities we considered. These thresholds correspond to the liquid-gas phase
612 transition in a lattice fluid, both in 2D [92] and 3D [93], and they are in good agreement
613 with theoretical mean-field calculations. Therefore, we choose E_{prey} and $E_{predator}$
614 above these thresholds, while not exceeding a few kT. In practice we take $3kT$. Then
615 E_{cross} should be either the same for matching T4P, or smaller otherwise, and we vary it
616 in the latter case.
617
618 *Killing by T6SS*
619 A predator can kill a neighbouring prey at rate k_{kill}. Once a killing event occurs, the
620 prey enters a lysing state, and is removed from the system at a certain rate k_{lysis}. For
621 simplicity, it is assumed that, while lysing, a prey moves and interacts with other
622 bacteria in the same way it did before being killed. However, it is unable to divide. The
623 values $k_{kill} = 6.25h^{-1}$ (total firing rate $k_{fire} = 50h^{-1}$ divided by the 8 possible firing
624 directions in the lattice) and $k_{lysis} = 75min^{-1}$ were chosen based on the ranges found
625 in the literature [64,65].
626
627 *Initial density*
628 In experiments, the average initial inoculum comprises 10^7 bacteria in 2 mL of solution,
629 and the induction of T4P and T6SS production continues for 3 hours until the
630 observation of aggregates at the 3.5-hour time point (Fig. 1E). Therefore, assuming
631 exponential growth at a rate $1.58h^{-1}$, the density at the onset of aggregation is
632 estimated to be around 10^9 bacteria per mL. In our 3D simulations, a $40\times40\times40$ body-
633 centred cubic lattice was considered, and the initial population consisted of 100 bacteria
634 (comprising half prey and half predators as in the experiments), resulting in

bioRxiv preprint doi: https://doi.org/10.1101/2023.10.25.564063; this version posted October 26, 2023. The copyright holder for this preprint (which was not certified by peer review) is the author/funder, who has granted bioRxiv a license to display the preprint in perpetuity. It is made available under aCC-BY-ND 4.0 International license.

635 approximately $100/(40 \times 4R/\sqrt{3})^3 \approx 10^9$ bacteria per mL, where R represents the
636 effective radius of a bacterium (see above).
637
638 *Simulation methods*
639 The simulations are conducted using a kinetic Monte Carlo algorithm [90]. Time is
640 discretized with a timestep chosen to ensure that it is unlikely that substantially more
641 than one event occurs within a step, typically on the order of 1 microsecond. Periodic
642 boundary conditions are applied.
643
644 *Assortment: quantitative characterization of mixing within aggregates*
645 Denoting prey by A and predators by B, we define assortment as $n_{AB}/n_{AB,\,max}$, where
646 n_{AB} is the number of adjacent prey-predator pairs, while $n_{AB,max}$ is its maximum
647 expected value, obtained if all bacteria were randomly mixed and in the bulk of an
648 aggregate. The latter is $n_{AB,max} = n_A \times 8 \times n_B/(n_A + n_B)$, namely the number of prey,
649 times the number of neighbouring sites it has in the lattice (8), times the probability that
650 a neighbouring site is occupied by a predator, assuming that all neighbouring sites are
651 occupied (which is the case in the aggregate bulk), and that prey and predators are
652 randomly mixed. Note that lysing prey are counted as prey in the calculation of
653 assortment.
654
655 **Bioinformatical analysis and phylogeny**
656 *Vibrio* spp. genomes used in this study are detailed in Supplementary Table 2. Any
657 genomes that were not previously annotated were annotated using the prokaryotic
658 genome annotation pipeline (PGAP, 2022-10-03. build6384) [94]. To reconstruct the
659 evolutionary history of the studied strains, we first assembled their pangenome along

bioRxiv preprint doi: https://doi.org/10.1101/2023.10.25.564063; this version posted October 26, 2023. The copyright holder for this preprint (which was not certified by peer review) is the author/funder, who has granted bioRxiv a license to display the preprint in perpetuity. It is made available under aCC-BY-ND 4.0 International license.

660 with a *V. mimicus* strain. We used PPanGGOLiN (v. 1.2.74) [95] and provided both
661 sequences and annotation to the program, while the rest of the parameters were set to
662 default. 1186 core genes were identified across the strains. We provided the core genes
663 to Modelfinder [96] to assess gene-specific optimal evolutionary models. Finally, the
664 phylogenetic reconstruction was performed using iqtree2 (v. 2.2.0) [97]. *V. mimicus* was
665 set as the outgroup and 100 bootstraps were computed in iqtree2. Nodes with bootstrap
666 values under 60 were collapsed using the collapseUnsupportedEdges function in the ips
667 package (v. 0.0.11, R environment) [98,99]. GC content was analysed by SnapGene (v.
668 4.3.11).

669 T6SS clusters in each genome were identified through blast analysis. A
670 nucleotide database was created using all the studied genomes by employing the
671 makeblastdb command (v. 2.12) with default parameters. The conserved flanking genes
672 for each T6SS cluster were selected based on their known arrangement. These genes
673 were then used as boundaries to identify the T6SS clusters within the genomes. The
674 A1552 sequences were used as query sequences (blastn, default parameters, e-value 1e-
675 10) to detect each respective cluster in the other strains, including the large cluster and
676 auxiliary clusters 1 to 3. For auxiliary clusters 4 and 5, we utilized the same approach
677 using the sequences from *V. cholerae* strain S12 [40] and *V. cholerae* strain BC1071
678 [41], respectively, as query.

679 To assess the different families and subfamilies of individual clusters, we
680 selected core immunity proteins for each cluster. These immunity protein sequences
681 were then aligned using muscle (v. 5.1.osx64, default parameters). The hierarchical
682 clustering and the identity matrices for each T6SS cluster were computed in an *R*
683 environment (v. 4.2.1), using the filter.identity function (cutoff = 0.3) in bio3d package
684 (v. 2.4-4). Heatmaps were then visualized with the pheatmap function (v. 1.0.12).

bioRxiv preprint doi: https://doi.org/10.1101/2023.10.25.564063; this version posted October 26, 2023. The copyright holder for this preprint (which was not certified by peer review) is the author/funder, who has granted bioRxiv a license to display the preprint in perpetuity. It is made available under aCC-BY-ND 4.0 International license.

685 The PilA nucleotide and protein sequences were collected based on the genome
686 annotations for each strain. A phylogenetic tree of the *pilA* nucleotide sequences of the
687 studied strains was reconstructed using iqtree2 (v. 2.2.0), and its statistical relevance
688 was asserted with 100 bootstraps. The best model of evolution was determined using
689 ModelFinder. Nodes with bootstrap values below 60 were collapsed using the
690 collapseUnsupportedEdges function. The protein sequences were aligned using muscle,
691 and the identity matrix was obtained in the *R* environment through the seqidentity
692 function in the bio3d package (v. 2.4-4). The resulting heatmap was visualised with the
693 pheatmap function (v. 1.0.12).
694
695 **Statistics and reproducibility**
696 All data represent the outcome of three independent biological experiments,
697 demonstrating consistent results. Bar graphs illustrate the mean value, with error bars
698 denoting the standard deviation. For scatter dot plots, lines represent the mean value.
699 Statistical analyses were conducted using GraphPad Prism (v. 9.1.2). Differences were
700 assessed using one-way ANOVA ($\alpha = 0.05$) and adjusted for multiple comparisons by
701 the Tukey post hoc test or by a two-tailed Student's t-test ($\alpha = 0.05$), when appropriate.
702
703 **Data availability**
704 Source data are provided with this paper.
705
706 **Code availability**
707 All simulation codes are available on GitHub: https://github.com/Bitbol-Lab/T4P-
708 T6SS-interplay
709

bioRxiv preprint doi: https://doi.org/10.1101/2023.10.25.564063; this version posted October 26, 2023. The copyright holder for this preprint (which was not certified by peer review) is the author/funder, who has granted bioRxiv a license to display the preprint in perpetuity. It is made available under aCC-BY-ND 4.0 International license.

710 ## Acknowledgements

711 We thank M. Jaskólska for provision of the codon-optimized mCherry construct, M.
712 Jaskólska & David W. Adams for their contribution to the mentoring of S.B.O. and
713 members of the Blokesch and Bitbol laboratory for fruitful discussions. This work was
714 supported by grants from the Swiss National Science Foundation (310030_185022) and
715 the European Research Council (724630) and an International Research Scholarship by
716 the Howard Hughes Medical Institute awarded to M.B. (55008726). R. S. and A.-F. B.
717 acknowledge funding from the European Research Council (ERC) under the European
718 Union's Horizon 2020 research and innovation programme (grant agreement No.
719 851173, to A.-F. B.).

720

721 ## Author contributions

722 S.B.O and M.B. conceived the project, designed and analysed the biological
723 experiments. S.B.O. constructed strains and plasmids and performed all biological
724 experiments. R.S. and A.-F.B. designed and analysed the computational model and the
725 numerical simulations. R.S. performed all numerical simulations. A.L. performed
726 bioinformatic analyses. S.B.O. and M.B. wrote the manuscript with input from A.L.,
727 R.S., and A.-F.B. M.B. and A.-F.B. acquired funding and supervised the project.

728

729 ## Conflicts of interest

730 The authors declare that there are no conflicts of interest

bioRxiv preprint doi: https://doi.org/10.1101/2023.10.25.564063; this version posted October 26, 2023. The copyright holder for this preprint (which was not certified by peer review) is the author/funder, who has granted bioRxiv a license to display the preprint in perpetuity. It is made available under aCC-BY-ND 4.0 International license.

731 **References**

732 1. Shin N-R, Whon TW, Bae J-W. Proteobacteria: microbial signature of dysbiosis
733 in gut microbiota. Trends Biotechnol. 2015;33: 496–503.
734 doi:10.1016/j.tibtech.2015.06.011
735 2. Zheng Q, Hu Y, Zhang S, Noll L, Böckle T, Dietrich M, et al. Soil
736 multifunctionality is affected by the soil environment and by microbial
737 community composition and diversity. Soil Biol Biochem. 2019;136: 107521.
738 doi:10.1016/j.soilbio.2019.107521
739 3. Foster KR, Bell T. Competition, Not Cooperation, Dominates Interactions among
740 Culturable Microbial Species. Current Biology. 2012;22: 1845–1850.
741 doi:10.1016/j.cub.2012.08.005
742 4. Ghoul M, Mitri S. The Ecology and Evolution of Microbial Competition. Trends
743 Microbiol. 2016;24: 833–845. doi:10.1016/j.tim.2016.06.011
744 5. Russel J, Røder HL, Madsen JS, Burmølle M, Sørensen SJ. Antagonism
745 correlates with metabolic similarity in diverse bacteria. Proceedings of the
746 National Academy of Sciences. 2017;114: 10684–10688.
747 doi:10.1073/pnas.1706016114
748 6. Smith WPJ, Wucher BR, Nadell CD, Foster KR. Bacterial defences:
749 mechanisms, evolution and antimicrobial resistance. Nat Rev Microbiol.
750 2023;21: 519–534. doi:10.1038/s41579-023-00877-3
751 7. García-Bayona L, Comstock LE. Bacterial antagonism in host-associated
752 microbial communities. Science (1979). 2018;361. doi:10.1126/science.aat2456
753 8. Klein TA, Ahmad S, Whitney JC. Contact-Dependent Interbacterial Antagonism
754 Mediated by Protein Secretion Machines. Trends Microbiol. 2020;28: 387–400.
755 doi:10.1016/j.tim.2020.01.003

bioRxiv preprint doi: https://doi.org/10.1101/2023.10.25.564063; this version posted October 26, 2023. The copyright holder for this preprint (which was not certified by peer review) is the author/funder, who has granted bioRxiv a license to display the preprint in perpetuity. It is made available under aCC-BY-ND 4.0 International license.

756 9. Ikryannikova LN, Kurbatov LK, Gorokhovets N V, Zamyatnin AA. Contact-
757 Dependent Growth Inhibition in Bacteria: Do Not Get Too Close! Int J Mol Sci.
758 2020;21. doi:10.3390/ijms21217990
759 10. Speare L, Woo M, Dunn AK, Septer AN. A Putative Lipoprotein Mediates Cell-
760 Cell Contact for Type VI Secretion System-Dependent Killing of Specific
761 Competitors. mBio. 2022;13. doi:10.1128/mbio.03085-21
762 11. Coulthurst S. The Type VI secretion system: a versatile bacterial weapon.
763 Microbiology (N Y). 2019;165: 503–515. doi:10.1099/mic.0.000789
764 12. Bingle LEH, Bailey CM, Pallen MJ. Type VI secretion: a beginner's guide. Curr
765 Opin Microbiol. 2008;11: 3–8. doi:10.1016/j.mib.2008.01.006
766 13. McNally L, Bernardy E, Thomas J, Kalziqi A, Pentz J, Brown SP, et al. Killing
767 by Type VI secretion drives genetic phase separation and correlates with
768 increased cooperation. Nat Commun. 2017;8: 14371. doi:10.1038/ncomms14371
769 14. Robitaille S, Simmons EL, Verster AJ, McClure EA, Royce DB, Trus E, et al.
770 Community composition and the environment modulate the population dynamics
771 of type VI secretion in human gut bacteria. bioRxiv. 2023.
772 doi:10.1101/2023.02.20.529031
773 15. Rudzite M, Subramoni S, Endres RG, Filloux A. Effectiveness of *Pseudomonas*
774 *aeruginosa* type VI secretion system relies on toxin potency and type IV pili-
775 dependent interaction. PLoS Pathog. 2023;19: e1011428-.
776 doi:10.1371/journal.ppat.1011428
777 16. Borenstein DB, Ringel P, Basler M, Wingreen NS. Established Microbial
778 Colonies Can Survive Type VI Secretion Assault. PLoS Comput Biol. 2015;11.
779 doi:10.1371/journal.pcbi.1004520

bioRxiv preprint doi: https://doi.org/10.1101/2023.10.25.564063; this version posted October 26, 2023. The copyright holder for this preprint (which was not certified by peer review) is the author/funder, who has granted bioRxiv a license to display the preprint in perpetuity. It is made available under aCC-BY-ND 4.0 International license.

780 17. Unterweger D, Miyata ST, Bachmann V, Brooks TM, Mullins T, Kostiuk B, et
781 al. The *Vibrio cholerae* type VI secretion system employs diverse effector
782 modules for intraspecific competition. Nat Commun. 2014;5: 3549.
783 doi:10.1038/ncomms4549
784 18. Russell AB, Hood RD, Bui NK, LeRoux M, Vollmer W, Mougous JD. Type VI
785 secretion delivers bacteriolytic effectors to target cells. Nature. 2011;475: 343–
786 347. doi:10.1038/nature10244
787 19. Pukatzki S, McAuley SB, Miyata ST. The type VI secretion system: translocation
788 of effectors and effector-domains. Curr Opin Microbiol. 2009;12: 11–17.
789 doi:10.1016/j.mib.2008.11.010
790 20. Drebes Dörr NC, Blokesch M. Interbacterial competition and anti-predatory
791 behaviour of environmental *Vibrio cholerae* strains. Environ Microbiol. 2020;22:
792 4485–4504. doi:10.1111/1462-2920.15224
793 21. Toska J, Ho BT, Mekalanos JJ. Exopolysaccharide protects *Vibrio cholerae* from
794 exogenous attacks by the type 6 secretion system. Proceedings of the National
795 Academy of Sciences. 2018;115: 7997–8002. doi:10.1073/pnas.1808469115
796 22. Hersch SJ, Watanabe N, Stietz MS, Manera K, Kamal F, Burkinshaw B, et al.
797 Envelope stress responses defend against type six secretion system attacks
798 independently of immunity proteins. Nat Microbiol. 2020;5: 706–714.
799 doi:10.1038/s41564-020-0672-6
800 23. Flaugnatti N, Isaac S, Lemos Rocha LF, Stutzmann S, Rendueles O, Stoudmann
801 C, et al. Human commensal gut Proteobacteria withstand type VI secretion
802 attacks through immunity protein-independent mechanisms. Nat Commun.
803 2021;12: 5751. doi:10.1038/s41467-021-26041-0

bioRxiv preprint doi: https://doi.org/10.1101/2023.10.25.564063; this version posted October 26, 2023. The copyright holder for this preprint (which was not certified by peer review) is the author/funder, who has granted bioRxiv a license to display the preprint in perpetuity. It is made available under aCC-BY-ND 4.0 International license.

804 24. Basler M, Ho BT, Mekalanos JJ. Tit-for-Tat: Type VI Secretion System
805 Counterattack during Bacterial Cell-Cell Interactions. Cell. 2013;152: 884–894.
806 doi:10.1016/j.cell.2013.01.042
807 25. Guillemette R, Ushijima B, Jalan M, Häse CC, Azam F. Insight into the
808 resilience and susceptibility of marine bacteria to T6SS attack by *Vibrio cholerae*
809 and *Vibrio coralliilyticus*. PLoS One. 2020;15.
810 doi:10.1371/journal.pone.0227864
811 26. Sorroche FG, Spesia MB, Zorreguieta Á, Giordano W. A Positive Correlation
812 between Bacterial Autoaggregation and Biofilm Formation in Native
813 *Sinorhizobium meliloti* Isolates from Argentina. Appl Environ Microbiol.
814 2012;78: 4092–4101. doi:10.1128/AEM.07826-11
815 27. Kragh KN, Hutchison JB, Melaugh G, Rodesney C, Roberts A EL, Irie Y, et al.
816 Role of Multicellular Aggregates in Biofilm Formation. mBio. 2016;7.
817 doi:10.1128/mbio.00237-16
818 28. Alhede M, Lorenz M, Fritz BG, Jensen PØ, Ring HC, Bay L, et al. Bacterial
819 aggregate size determines phagocytosis efficiency of polymorphonuclear
820 leukocytes. Med Microbiol Immunol. 2020;209: 669–680. doi:10.1007/s00430-
821 020-00691-1
822 29. Caceres SM, Malcolm KC, Taylor-Cousar JL, Nichols DP, Saavedra MT, Bratton
823 DL, et al. Enhanced In Vitro Formation and Antibiotic Resistance of Nonattached
824 Pseudomonas aeruginosa Aggregates through Incorporation of Neutrophil
825 Products. Antimicrob Agents Chemother. 2014;58: 6851–6860.
826 doi:10.1128/aac.03514-14

bioRxiv preprint doi: https://doi.org/10.1101/2023.10.25.564063; this version posted October 26, 2023. The copyright holder for this preprint (which was not certified by peer review) is the author/funder, who has granted bioRxiv a license to display the preprint in perpetuity. It is made available under aCC-BY-ND 4.0 International license.

827 30. Corno G, Coci M, Giardina M, Plechuk S, Campanile F, Stefani S. Antibiotics
828 promote aggregation within aquatic bacterial communities. Front Microbiol.
829 2014;5. doi:10.3389/fmicb.2014.00297
830 31. Trunk T, Khalil HS, Leo JC. Bacterial autoaggregation. AIMS Microbiol.
831 2018;4: 140–164. doi:10.3934/microbiol.2018.1.140
832 32. Ligthart K, Belzer C, de Vos WM, Tytgat HLP. Bridging Bacteria and the Gut:
833 Functional Aspects of Type IV Pili. Trends Microbiol. 2020;28: 340–348.
834 doi:10.1016/j.tim.2020.02.003
835 33. Ellison CK, Whitfield GB, Brun Y V. Type IV Pili: dynamic bacterial
836 nanomachines. FEMS Microbiol Rev. 2022;46. doi:10.1093/femsre/fuab053
837 34. Craig L, Forest KT, Maier B. Type IV pili: dynamics, biophysics and functional
838 consequences. Nat Rev Microbiol. 2019;17: 429–440. doi:10.1038/s41579-019-
839 0195-4
840 35. Taylor RK, Miller VL, Furlong DB, Mekalanos JJ. Use of phoA gene fusions to
841 identify a pilus colonization factor coordinately regulated with cholera toxin.
842 Proc Natl Acad Sci U S A. 1987;84: 2833–2837. doi:10.1073/pnas.84.9.2833
843 36. O'Toole GA, Kolter R. Flagellar and twitching motility are necessary for
844 *Pseudomonas aeruginosa* biofilm development. Mol Microbiol. 1998;30: 295–
845 304. doi:10.1046/j.1365-2958.1998.01062.x
846 37. Carbonnelle E, Helaine S, Nassif X, Pelicic V. A systematic genetic analysis in
847 *Neisseria meningitidis* defines the Pil proteins required for assembly,
848 functionality, stabilization and export of type IV pili. Mol Microbiol. 2006;61:
849 1510–1522. doi:10.1111/j.1365-2958.2006.05341.x

bioRxiv preprint doi: https://doi.org/10.1101/2023.10.25.564063; this version posted October 26, 2023. The copyright holder for this preprint (which was not certified by peer review) is the author/funder, who has granted bioRxiv a license to display the preprint in perpetuity. It is made available under aCC-BY-ND 4.0 International license.

850 38. Owen P, Meehan M, de Loughry-Doherty H, Henderson I. Phase-variable outer
851 membrane proteins in *Escherichia coli*. FEMS Immunol Med Microbiol.
852 1996;16: 63–76. doi:10.1111/j.1574-695X.1996.tb00124.x
853 39. Altindis E, Dong T, Catalano C, Mekalanos J. Secretome Analysis of *Vibrio*
854 *cholerae* Type VI Secretion System Reveals a New Effector-Immunity Pair.
855 mBio. 2015;6. doi:10.1128/mbio.00075-15
856 40. Labbate M, Orata FD, Petty NK, Jayatilleke ND, King WL, Kirchberger PC, et
857 al. A genomic island in *Vibrio cholerae* with VPI-1 site-specific recombination
858 characteristics contains CRISPR-Cas and type VI secretion modules. Sci Rep.
859 2016;6: 36891. doi:10.1038/srep36891
860 41. Crisan C V, Chande AT, Williams K, Raghuram V, Rishishwar L, Steinbach G,
861 et al. Analysis of *Vibrio cholerae* genomes identifies new type VI secretion
862 system gene clusters. Genome Biol. 2019;20: 163. doi:10.1186/s13059-019-
863 1765-5
864 42. Meibom KL, Blokesch M, Dolganov NA, Wu CY, Schoolnik GK. Microbiology:
865 Chitin induces natural competence in *Vibrio cholerae*. Science (1979). 2005;310:
866 1824–1827. doi:10.1126/science.1120096
867 43. Borgeaud S, Metzger LC, Scrignari T, Blokesch M. The type VI secretion system
868 of *Vibrio cholerae* fosters horizontal gene transfer. Science (1979). 2015;347:
869 63–67. doi:10.1126/science.1260064
870 44. Matthey N, Stutzmann S, Stoudmann C, Guex N, Iseli C, Blokesch M. Neighbor
871 predation linked to natural competence fosters the transfer of large genomic
872 regions in *Vibrio cholerae*. Elife. 2019;8. doi:10.7554/eLife.48212

bioRxiv preprint doi: https://doi.org/10.1101/2023.10.25.564063; this version posted October 26, 2023. The copyright holder for this preprint (which was not certified by peer review) is the author/funder, who has granted bioRxiv a license to display the preprint in perpetuity. It is made available under aCC-BY-ND 4.0 International license.

873 45. Watve SS, Thomas J, Hammer BK. CytR Is a Global Positive Regulator of
874 Competence, Type VI Secretion, and Chitinases in *Vibrio cholerae*. PLoS One.
875 2015;10: e0138834-. doi:10.1371/journal.pone.0138834
876 46. Jaskolska M, Stutzmann S, Stoudmann C, Blokesch M. QstR-dependent
877 regulation of natural competence and type VI secretion in *Vibrio cholerae*.
878 Nucleic Acids Res. 2018;46: 10619–10634. doi:10.1093/nar/gky717
879 47. Unterweger D, Kitaoka M, Miyata ST, Bachmann V, Brooks TM, Moloney J, et
880 al. Constitutive Type VI Secretion System Expression Gives *Vibrio cholerae*
881 Intra- and Interspecific Competitive Advantages. PLoS One. 2012;7: e48320-.
882 doi:10.1371/journal.pone.0048320
883 48. Bernardy EE, Turnsek MA, Wilson SK, Tarr CL, Hammer BK. Diversity of
884 Clinical and Environmental Isolates of *Vibrio cholerae* in Natural Transformation
885 and Contact-Dependent Bacterial Killing Indicative of Type VI Secretion System
886 Activity. Appl Environ Microbiol. 2016;82: 2833–2842.
887 doi:10.1128/AEM.00351-16
888 49. Drebes Dörr NC, Proutière A, Jaskólska M, Stutzmann S, Bader L, Blokesch M.
889 Single nucleotide polymorphism determines constitutive versus inducible type VI
890 secretion in *Vibrio cholerae*. ISME J. 2022;16: 1868–1872. doi:10.1038/s41396-
891 022-01234-7
892 50. Ng SL, Kammann S, Steinbach G, Hoffmann T, Yunker PJ, Hammer BK.
893 Evolution of a *cis*-Acting SNP That Controls Type VI Secretion in *Vibrio*
894 *cholerae*. mBio. 2022;13: e00422-22. doi:10.1128/mbio.00422-22
895 51. Adams DW, Stutzmann S, Stoudmann C, Blokesch M. DNA-uptake pili of
896 *Vibrio cholerae* are required for chitin colonization and capable of kin

bioRxiv preprint doi: https://doi.org/10.1101/2023.10.25.564063; this version posted October 26, 2023. The copyright holder for this preprint (which was not certified by peer review) is the author/funder, who has granted bioRxiv a license to display the preprint in perpetuity. It is made available under aCC-BY-ND 4.0 International license.

897 recognition via sequence-specific self-interaction. Nat Microbiol. 2019;4: 1545–
898 1557. doi:10.1038/s41564-019-0479-5
899 52. Giltner CL, Nguyen Y, Burrows LL. Type IV Pilin Proteins: Versatile Molecular
900 Modules. Microbiology and Molecular Biology Reviews. 2012;76: 740–772.
901 doi:10.1128/mmbr.00035-12
902 53. Aagesen AM, Häse CC. Sequence Analyses of Type IV Pili from *Vibrio*
903 *cholerae*, *Vibrio parahaemolyticus*, and *Vibrio vulnificus*. Microb Ecol. 2012;64:
904 509–524. doi:10.1007/s00248-012-0021-2
905 54. Ronish LA, Lillehoj E, Fields JK, Sundberg EJ, Piepenbrink KH. The structure
906 of PilA from *Acinetobacter baumannii* AB5075 suggests a mechanism for
907 functional specialization in *Acinetobacter* type IV pili. Journal of Biological
908 Chemistry. 2019;294: 218–230. doi:10.1074/jbc.RA118.005814
909 55. Pukatzki S, Ma AT, Sturtevant D, Krastins B, Sarracino D, Nelson WC, et al.
910 Identification of a conserved bacterial protein secretion system in *Vibrio cholerae*
911 using the *Dictyostelium* host model system. Proceedings of the National
912 Academy of Sciences. 2006;103: 1528–1533. doi:10.1073/pnas.0510322103
913 56. Hélaine S, Carbonnelle E, Prouvensier L, Beretti J-L, Nassif X, Pelicic V. PilX, a
914 pilus-associated protein essential for bacterial aggregation, is a key to pilus-
915 facilitated attachment of *Neisseria meningitidis* to human cells. Mol Microbiol.
916 2005;55: 65–77. doi:10.1111/j.1365-2958.2004.04372.x
917 57. Travisano M, Lenski RE. Long-Term Experimental Evolution in *Escherichia*
918 *coli*. IV. Targets of Selection and the Specificity of Adaptation. Genetics.
919 1996;143: 15–26. doi:10.1093/genetics/143.1.15

bioRxiv preprint doi: https://doi.org/10.1101/2023.10.25.564063; this version posted October 26, 2023. The copyright holder for this preprint (which was not certified by peer review) is the author/funder, who has granted bioRxiv a license to display the preprint in perpetuity. It is made available under aCC-BY-ND 4.0 International license.

920 58. Ringel PD, Hu D, Basler M. The Role of Type VI Secretion System Effectors in
921 Target Cell Lysis and Subsequent Horizontal Gene Transfer. Cell Rep. 2017;21:
922 3927–3940. doi:10.1016/j.celrep.2017.12.020
923 59. Ting S-Y, Martínez-García E, Huang S, Bertolli SK, Kelly KA, Cutler KJ, et al.
924 Targeted Depletion of Bacteria from Mixed Populations by Programmable
925 Adhesion with Antagonistic Competitor Cells. Cell Host Microbe. 2020;28: 313-
926 321.e6. doi:10.1016/j.chom.2020.05.006
927 60. Custodio R, Ford RM, Ellison CJ, Liu G, Mickute G, Tang CM, et al. Type VI
928 secretion system killing by commensal *Neisseria* is influenced by expression of
929 type four pili. Elife. 2021;10. doi:10.7554/eLife.63755
930 61. Kirchberger PC, Unterweger D, Provenzano D, Pukatzki S, Boucher Y.
931 Sequential displacement of Type VI Secretion System effector genes leads to
932 evolution of diverse immunity gene arrays in *Vibrio cholerae*. Sci Rep. 2017;7:
933 45133. doi:10.1038/srep45133
934 62. Salomon D, Klimko JA, Trudgian DC, Kinch LN, Grishin N V., Mirzaei H, et al.
935 Type VI Secretion System Toxins Horizontally Shared between Marine Bacteria.
936 Mougous JD, editor. PLoS Pathog. 2015;11: e1005128.
937 doi:10.1371/journal.ppat.1005128
938 63. Wielert I, Kraus-Römer S, Volkmann TE, Craig L, Higgins PG, Maier B.
939 Antigenic variation impacts gonococcal lifestyle and antibiotic tolerance by
940 modulating interbacterial forces. bioRxiv. 2023. doi:10.1101/2023.07.06.548055
941 64. Smith WPJ, Vettiger A, Winter J, Ryser T, Comstock LE, Basler M, et al. The
942 evolution of the type VI secretion system as a disintegration weapon. Sourjik V,
943 editor. PLoS Biol. 2020;18. doi:10.1371/journal.pbio.3000720

bioRxiv preprint doi: https://doi.org/10.1101/2023.10.25.564063; this version posted October 26, 2023. The copyright holder for this preprint (which was not certified by peer review) is the author/funder, who has granted bioRxiv a license to display the preprint in perpetuity. It is made available under aCC-BY-ND 4.0 International license.

944 65. Smith WPJ, Brodmann M, Unterweger D, Davit Y, Comstock LE, Basler M, et
945 al. The evolution of tit-for-tat in bacteria via the type VI secretion system. Nat
946 Commun. 2020;11: 5395. doi:10.1038/s41467-020-19017-z
947 66. Jude BA, Taylor RK. The physical basis of type 4 pilus-mediated microcolony
948 formation by *Vibrio cholerae* O1. J Struct Biol. 2011;175: 1–9.
949 doi:10.1016/j.jsb.2011.04.008
950 67. Giltner CL, Nguyen Y, Burrows LL. Type IV Pilin Proteins: Versatile Molecular
951 Modules. Microbiology and Molecular Biology Reviews. 2012;76: 740–772.
952 doi:10.1128/mmbr.00035-12
953 68. Yildiz FH, Schoolnik GK. Role of rpoS in stress survival and virulence of *Vibrio*
954 *cholerae*. J Bacteriol. 1998;180: 773–784. doi:10.1128/jb.180.4.773-784.1998
955 69. Matthey N, Drebes Dörr N, Blokesch M. Long-Read-Based Genome Sequences
956 of Pandemic and Environmental *Vibrio cholerae* Strains. Microbiol Resour
957 Announc. 2018;7. doi:10.1128/MRA.01574-18
958 70. Wee S, Wilkinson BJ. Increased outer membrane ornithine-containing lipid and
959 lysozyme penetrability of *Paracoccus denitrificans* grown in a complex medium
960 deficient in divalent cations. J Bacteriol. 1988;170: 3283–3286.
961 doi:10.1128/jb.170.7.3283-3286.1988
962 71. Tang M-X, Pei T-T, Xiang Q, Wang Z-H, Luo H, Wang X-Y, et al. Abiotic
963 factors modulate interspecies competition mediated by the type VI secretion
964 system effectors in *Vibrio cholerae*. ISME J. 2022;16: 1765–1775.
965 doi:10.1038/s41396-022-01228-5
966 72. Mewes A, Langer G, de Nooijer LJ, Bijma J, Reichart G-J. Effect of different
967 seawater Mg2+ concentrations on calcification in two benthic foraminifers. Mar
968 Micropaleontol. 2014;113: 56–64. doi:10.1016/j.marmicro.2014.09.003

bioRxiv preprint doi: https://doi.org/10.1101/2023.10.25.564063; this version posted October 26, 2023. The copyright holder for this preprint (which was not certified by peer review) is the author/funder, who has granted bioRxiv a license to display the preprint in perpetuity. It is made available under aCC-BY-ND 4.0 International license.

969 73. LaCourse KD, Peterson SB, Kulasekara HD, Radey MC, Kim J, Mougous JD.
970 Conditional toxicity and synergy drive diversity among antibacterial effectors.
971 Nat Microbiol. 2018;3: 440–446. doi:10.1038/s41564-018-0113-y
972 74. Lambertsen L, Sternberg C, Molin S. Mini-Tn7 transposons for site-specific
973 tagging of bacteria with fluorescent proteins. Environ Microbiol. 2004;6: 726–
974 732. doi:10.1111/j.1462-2920.2004.00605.x
975 75. Sambrook J, Fritsch EF, Maniatis T. Molecular cloning: a laboratory manual.
976 Cold spring harbor laboratory press; 1989.
977 76. De Souza Silva O, Blokesch M. Genetic manipulation of *Vibrio cholerae* by
978 combining natural transformation with FLP recombination. Plasmid. 2010;64:
979 186–195. doi:10.1016/j.plasmid.2010.08.001
980 77. Marvig RL, Blokesch M. Natural transformation of *Vibrio cholerae* as a tool -
981 Optimizing the procedure. BMC Microbiol. 2010;10: 155. doi:10.1186/1471-
982 2180-10-155
983 78. Blokesch M. TransFLP — A Method to Genetically Modify *Vibrio cholerae*
984 Based on Natural Transformation and FLP-recombination. Journal of Visualized
985 Experiments. 2012; e3761. doi:10.3791/3761
986 79. Bao Y, Lies DP, Fu H, Roberts GP. An improved Tn7-based system for the
987 single-copy insertion of cloned genes into chromosomes of gram-negative
988 bacteria. Gene. 1991;109: 167–168. doi:10.1016/0378-1119(91)90604-A
989 80. Meibom KL, Li XB, Nielsen AT, Wu C-Y, Roseman S, Schoolnik GK. The
990 *Vibrio cholerae* chitin utilization program. Proceedings of the National Academy
991 of Sciences. 2004;101: 2524–2529. doi:10.1073/pnas.0308707101

bioRxiv preprint doi: https://doi.org/10.1101/2023.10.25.564063; this version posted October 26, 2023. The copyright holder for this preprint (which was not certified by peer review) is the author/funder, who has granted bioRxiv a license to display the preprint in perpetuity. It is made available under aCC-BY-ND 4.0 International license.

992 81. Jaskólska M, Adams DW, Blokesch M. Two defence systems eliminate plasmids
993 from seventh pandemic *Vibrio cholerae*. Nature. 2022;604: 323–329.
994 doi:10.1038/s41586-022-04546-y
995 82. Lenski RE, Rose MR, Simpson SC, Tadler SC. Long-Term Experimental
996 Evolution in *Escherichia coli*. I. Adaptation and Divergence During 2,000
997 Generations. Am Nat. 1991;138: 1315–1341. doi:10.1086/285289
998 83. Schindelin J, Arganda-Carreras I, Frise E, Kaynig V, Longair M, Pietzsch T, et
999 al. Fiji: an open-source platform for biological-image analysis. Nat Methods.
1000 2012;9: 676–682. doi:10.1038/nmeth.2019
1001 84. Taylor GI. Diffusion by Continuous Movements. Proceedings of the London
1002 Mathematical Society. 1922;s2-20: 196–212. doi:10.1112/plms/s2-20.1.196
1003 85. Tchen CM. Diffusion of Particles in Turbulent Flow. Advances in Geophysics.
1004 Elsevier; 1959. pp. 165–174. doi:10.1016/S0065-2687(08)60103-X
1005 86. Roberts PJ, Webster DR. Turbulent diffusion. Environmental Fluid Mechanics
1006 Theories and Application. Reston, Virginia: ASCE Press; 2002. Available:
1007 https://www.astro.princeton.edu/~burrows/classes/542/papers/Alwin.Roberts_Tu
1008 rb_Diffusion-1.pdf
1009 87. Lovely PS, Dahlquist FW. Statistical measures of bacterial motility and
1010 chemotaxis. J Theor Biol. 1975;50: 477–496. doi:10.1016/0022-5193(75)90094-
1011 6
1012 88. Lemos Rocha LF, Peters K, Biboy J, Depelteau JS, Briegel A, Vollmer W, et al.
1013 The VarA-CsrA regulatory pathway influences cell shape in *Vibrio cholerae*.
1014 PLoS Genet. 2022;18. doi:10.1371/journal.pgen.1010143

bioRxiv preprint doi: https://doi.org/10.1101/2023.10.25.564063; this version posted October 26, 2023. The copyright holder for this preprint (which was not certified by peer review) is the author/funder, who has granted bioRxiv a license to display the preprint in perpetuity. It is made available under aCC-BY-ND 4.0 International license.

1015 89. Grognot M, Mittal A, Mah'moud M, Taute KM. *Vibrio cholerae* Motility in
1016 Aquatic and Mucus-Mimicking Environments. Appl Environ Microbiol.
1017 2021;87: e0129321. doi:10.1128/AEM.01293-21
1018 90. Landau DP, Binder K. A Guide to Monte Carlo Simulations in Statistical
1019 Physics. Cambridge University Press; 2021. doi:10.1017/9781108780346
1020 91. Thomen P, Valentin JDP, Bitbol A-F, Henry N. Spatiotemporal pattern formation
1021 in *E. coli* biofilms explained by a simple physical energy balance. Soft Matter.
1022 2020;16: 494–504. doi:10.1039/C9SM01375J
1023 92. Bittner E, Janke W. A boundary field induced first-order transition in the 2D
1024 Ising model: numerical study. J Phys A Math Theor. 2008;41. doi:10.1088/1751-
1025 8113/41/39/395001
1026 93. Blöte HWJ, Heringa JR, Tsypin MM. Three-dimensional Ising model in the
1027 fixed-magnetization ensemble: A Monte Carlo study. Phys Rev E. 2000;62: 77–
1028 82. doi:10.1103/PhysRevE.62.77
1029 94. Tatusova T, DiCuccio M, Badretdin A, Chetvernin V, Nawrocki EP, Zaslavsky
1030 L, et al. NCBI prokaryotic genome annotation pipeline. Nucleic Acids Res.
1031 2016;44: 6614–6624. doi:10.1093/nar/gkw569
1032 95. Gautreau G, Bazin A, Gachet M, Planel R, Burlot L, Dubois M, et al.
1033 PPanGGOLiN: Depicting microbial diversity via a partitioned pangenome graph.
1034 PLoS Comput Biol. 2020;16. doi:10.1371/journal.pcbi.1007732
1035 96. Kalyaanamoorthy S, Minh BQ, Wong TKF, von Haeseler A, Jermiin LS.
1036 ModelFinder: fast model selection for accurate phylogenetic estimates. Nat
1037 Methods. 2017;14: 587–589. doi:10.1038/nmeth.4285
1038 97. Minh BQ, Schmidt HA, Chernomor O, Schrempf D, Woodhams MD, von
1039 Haeseler A, et al. IQ-TREE 2: New Models and Efficient Methods for

bioRxiv preprint doi: https://doi.org/10.1101/2023.10.25.564063; this version posted October 26, 2023. The copyright holder for this preprint (which was not certified by peer review) is the author/funder, who has granted bioRxiv a license to display the preprint in perpetuity. It is made available under aCC-BY-ND 4.0 International license.

1040 Phylogenetic Inference in the Genomic Era. Mol Biol Evol. 2020;37: 1530–1534.
1041 doi:10.1093/molbev/msaa015
1042 98. Heibl C. PHYLOCH: R language tree plotting tools and interfaces to diverse
1043 phylogenetic software packages. 2008. Available:
1044 http://www.christophheibl.de/Rpackages.html
1045 99. R Core Team. R: A Language and Environment for Statistical Computing,
1046 Vienna, Austria. 2021. Available: https://www.R-project.org/
1047
1048

bioRxiv preprint doi: https://doi.org/10.1101/2023.10.25.564063; this version posted October 26, 2023. The copyright holder for this preprint (which was not certified by peer review) is the author/funder, who has granted bioRxiv a license to display the preprint in perpetuity. It is made available under aCC-BY-ND 4.0 International license.

1049 # Figure legends

1050 **Fig. 1. T4P facilitate T6SS-mediated killing in liquid by promoting**
1051 **autoaggregation. A)** Selection rates of T6SS-competent (Parent) and non-functional
1052 (Δ*vasK*) predator strains when co-cultured with T6SS-sensitive (Δ4E/I) prey strains.
1053 Both prey and predator strains carry their native major pilin gene (*pilA* (A1552)) or lack
1054 it (Δ*pilA*). Selection rates were determined after 6 h of growth. **B)** Representative
1055 microscopy images of 4-hour-old co-cultures, corresponding to the experiment in (A).
1056 The images include phase contrast (left), a merged view of prey (sfGFP, in green) and
1057 predator strains (mCherry, in red) (middle), and SYTOX Blue dead cell stain (in blue)
1058 (right). An inset provides a zoomed-in view of an aggregate indicated on the phase
1059 channel by a white box. White scalebar: 25 µm. **C)** Zoomed snapshots taken after 1 h
1060 from simulations conducted as described in the methods section. The simulations
1061 consider T4P self-interactions (left vs. right column) and T6SS-mediated killing (top vs.
1062 bottom row) either enabled or disabled. Prey and predator cells are represented by green
1063 and red markers, respectively, while lysing cells are indicated by black markers. The
1064 black scale bar indicates the length of 5 marker diameters. In the “no T4P” panels, we
1065 display the content of an arbitrary cube, of edge about 23 cell diameters, extracted from
1066 the system. **D)** Time-course analysis of selection rates of predator strains in co-culture
1067 experiments, comparing *pilA*-carrying co-cultures to corresponding *pilA*-deleted co-
1068 cultures. **E)** Time-course of co-culture experiments demonstrating the aggregation level
1069 at indicated incubation times. The aggregation level is determined by the ratio of the co-
1070 culture’s optical density at 600 nm (OD_{600}) pre/post-vortex. The horizontal dotted line
1071 represents the value around which no aggregation occurs. Graphs show the mean, with
1072 error bars giving the standard deviation; circles represent data from three independent
1073 experiments. In dot plots, significant differences were determined using one-way

bioRxiv preprint doi: https://doi.org/10.1101/2023.10.25.564063; this version posted October 26, 2023. The copyright holder for this preprint (which was not certified by peer review) is the author/funder, who has granted bioRxiv a license to display the preprint in perpetuity. It is made available under aCC-BY-ND 4.0 International license.

1074 ANOVA with Tukey's post hoc test (****P* < 0.001). *P* values are provided in the source
1075 data file.
1076
1077 **Fig. 2. Conservation of T4P-Mediated T6SS Killing Across Self-Interacting PilA**
1078 **Variants. A)** Cladogram presenting 39 *V. cholerae* strains analysed based on 1186 core
1079 genes. *V. mimicus* (ATCC33655) is used as an outgroup. Statistical support is evaluated
1080 through 100 bootstraps, with nodes below 60 being collapsed. T6SS effector module
1081 families in the large- and auxiliary clusters (LC, Aux 1-5) are specified behind the strain
1082 names, followed by the self-interaction ability of T4P. **B)** Bacterial competition assay
1083 introducing self-interacting PilA variants into T6SS-competent (predator) and T6SS-
1084 sensitive (prey) strains. **C)** Selection rate of non-interacting PilA variants, with self-
1085 interacting *pilA*rep[A1552] serving as a positive control. **D)** Aggregation assay
1086 assessing the aggregation level of PilA variants SL6Y and DRC186. Cultures are
1087 allowed to settle for the specified duration, after which the aggregation level was
1088 determined by calculating the ratio of the culture's OD_{600} before and after vortexing.
1089 The horizontal dotted line denotes the ratio around which no aggregation occurs. Δ*pilA*
1090 and *pilA*rep[A1552] are designated as negative and positive controls, respectively.
1091 Circles in graphs represent independent replicates, while bars/lines indicate the mean,
1092 with error bars illustrating the standard deviation. Selection rates of predators were
1093 compared to Δ*pilA* for statistical analysis (ANOVA with Tukey's post hoc test; *** *P* <
1094 0.001). *P* values are provided in the source data file.
1095
1096 **Fig. 3. Impact of Pilus Specificity on T6SS Competition and Spatial Segregation.**
1097 **A)** Selection rate of T6SS-competent (predator) strains competing with T6SS-sensitive
1098 (prey) strains, with diverse PilA variants among the prey strains, against a predator

bioRxiv preprint doi: https://doi.org/10.1101/2023.10.25.564063; this version posted October 26, 2023. The copyright holder for this preprint (which was not certified by peer review) is the author/funder, who has granted bioRxiv a license to display the preprint in perpetuity. It is made available under aCC-BY-ND 4.0 International license.

1099 strain carrying the A1552 PilA variant. **B)** Representative microscopy images of
1100 prey/predator co-cultures, exhibiting either matching (A1552 : A1552) or diverse (SP6G
1101 : A1552) PilA variants. Images include phase contrast, a merge of prey (sfGFP, in
1102 green) and predator strains (mCherry, in red), and SYTOX Blue dead cell stain (blue).
1103 The white scale bar denotes 25 µm. **C)** Snapshots from simulations after 1 h, with
1104 varied T4P-mediated binding energy (E_{cross}) between predators and prey. E_{cross} was
1105 set at $3kT$ for matching T4P and 0 for diverse T4P. **D)** Snapshots from simulations after
1106 1 h, representing various levels of T4P promiscuity obtained by modulating the T4P-
1107 mediated binding energy E_{cross}, compared to a matching T4P control. **E)** Selection rates
1108 in prey/predator co-culture experiments, where the carried PilA variants display
1109 differing levels of promiscuous T4P self-interactions. **F)** Imaging of co-culture
1110 experiments between T6SS-competent (predator) and T6SS-sensitive (prey) strains,
1111 featuring PilA variants with varying levels of promiscuousness. The left panel shows
1112 phase contrast, the middle panel displays a merge of prey (sfGFP, in green) and
1113 predator (mCherry, in red) strains, while the right panel exhibits SYTOX Blue dead cell
1114 stain (blue). The white scale bar indicates 25 µm. Circles in graphs represent
1115 independent experiments and means are indicated by lines. Statistical tests were
1116 compared with the (non-promiscuous) matching *pilA*rep[A1552] control condition using
1117 ANOVA with Tukey's post hoc test (*** $P < 0.001$). For simulations, prey and
1118 predators are represented by green and red markers, respectively. Lysing cells are
1119 denoted by black markers. The black scale bar indicates the length of 5 marker
1120 diameters.
1121
1122 **Fig. 4. Influence of Spatial Assortment and Lysis Time on T6SS-Mediated Target**
1123 **Depletion. A)** The impact of the attractive interaction between prey and predators on

bioRxiv preprint doi: https://doi.org/10.1101/2023.10.25.564063; this version posted October 26, 2023. The copyright holder for this preprint (which was not certified by peer review) is the author/funder, who has granted bioRxiv a license to display the preprint in perpetuity. It is made available under aCC-BY-ND 4.0 International license.

1124 mixing over time. The main panel displays the assortment between prey and predators
1125 over time for different values of the T4P binding energy E_{cross} between a prey and a
1126 predator. Solid lines represent simulations with killing ($k_{kill} = 6.25h^{-1}$), while dashed
1127 lines depict scenarios without killing ($k_{kill} = 0$). Assortment is determined by
1128 comparing the number of adjacent prey-predator pairs to its maximum expected value,
1129 considering lysing cells as prey (see methods). The inset graph shows assortment after 1
1130 h versus E_{cross}. **B)** Evolution of selection rate over time. The main panel depicts the
1131 mean selection rate versus time for various E_{cross} values. The inset showcases the
1132 frequency of fixation events, where only predators remain, and prey are completely
1133 depleted, across the replicate simulations. When fixation occurs in a replicate, its
1134 selection rate diverges, and is thus excluded from the calculation of the mean selection
1135 rate. To address potential bias, the results are displayed until the frequency of fixations
1136 reaches 0.25 for $E_{cross} = 3kT$. The shaded areas represent the interquartile ranges. **C)**
1137 The influence of attraction between prey and predators on the resulting predator
1138 selection rate. The graph displays the mean selection rate versus E_{cross} after 20 minutes
1139 of simulation. **D)** The effect of lysis time on prey depletion. The mean predator
1140 selection rate is shown versus the mean lysis time ($1/k_{lysis}$) after 20 minutes of
1141 simulation with $E_{cross} = 3kT$. When a fixation occurs in a replicate simulation, the
1142 corresponding selection rate diverges, and is therefore not considered in the calculation
1143 of the mean selection rate. Fixation events were observed in less than 0.5% of replicate
1144 simulations. All results are averaged over 10^3 replicate simulations.
1145
1146

bioRxiv preprint doi: https://doi.org/10.1101/2023.10.25.564063; this version posted October 26, 2023. The copyright holder for this preprint (which was not certified by peer review) is the author/funder, who has granted bioRxiv a license to display the preprint in perpetuity. It is made available under aCC-BY-ND 4.0 International license.

1147 ## Supplementary Figure legends

1148 **Fig. S1. Refinement of Bacterial Competition Assays. A)** Relative fitness of
1149 antibiotic/fluorescent marker-carrying strains used for the construction of predator and
1150 prey strains, competed against the control strain (A1552Δ*lacZ*). **B)** LB medium batch-
1151 to-batch variability in the aggregation level can be counteracted by the supplementation
1152 of divalent cations. The aggregation level is determined by the ratio of the culture's
1153 OD_{600} pre/post vortex. The horizontal dotted line represents the ratio around which no
1154 aggregation occurs. All presented values are the mean of 3 repeats, with error bars
1155 indicating the standard deviation. Significant differences were determined by a two-
1156 tailed Student's t-test.

1157

1158 **Fig. S2. Evolution over time of a simulated aggregate with matching T4P and T6SS**
1159 **killing.** The simulation is performed as described in the methods section, where all
1160 parameter values are given. Prey and predators are represented by green and red
1161 markers, respectively. Lysing cells are represented by black markers. Within each panel,
1162 the number of bacteria forming the aggregate of interest is indicated, and the black scale
1163 bar shows the length of 5 marker diameters. In the second panel (1 minute), we show
1164 two randomly chosen small aggregates (the dashed line separating the two plots
1165 indicates that they are not close to each other), but note that other aggregates or isolated
1166 bacteria later end up within the aggregate of interest. In the first panel (0 minute), we
1167 display the content of an arbitrary cube, of edge about 23 cell diameters, extracted from
1168 the system.

1169

1170 **Fig. S3. Comparison of Large Cluster-encoded Immunity Proteins.** The heat map
1171 displays the fraction identity (fraction of identical residues) among core immunity

bioRxiv preprint doi: https://doi.org/10.1101/2023.10.25.564063; this version posted October 26, 2023. The copyright holder for this preprint (which was not certified by peer review) is the author/funder, who has granted bioRxiv a license to display the preprint in perpetuity. It is made available under aCC-BY-ND 4.0 International license.

1172 proteins encoded in the T6SS large cluster (LC) from patient and environmental isolates
1173 used in this study, along with strain representatives of known families [17,61]. Green
1174 indicates a fraction identity of 1 (same family and subfamily), yellow indicates a
1175 fraction identity of >0.3 (same family), and red indicates a fraction identity of ≤0.3
1176 (different family). Families are labelled by letters on the side of the heatmap, and stars
1177 denote novel families. After manual inspection, SL6Y was classified into its own family
1178 as the identity values corresponding to family H were at the threshold level and did not
1179 encompass all of the family H strains.
1180
1181 **Fig. S4. Comparison of Auxiliary Cluster 1-encoded Immunity Proteins.** The heat
1182 map illustrates the fraction identity (fraction of identical residues) among core immunity
1183 proteins located in T6SS auxiliary cluster 1 (Aux1) from patient and environmental
1184 isolates used in this study, along with strain representatives of known families [17,61].
1185 Green indicates a fraction identity of 1 (same family and subfamily), yellow indicates a
1186 fraction identity of >0.3 (same family), and red indicates a fraction identity of ≤0.3
1187 (different family). Families are labelled by letters on the side of the heatmap.
1188
1189 **Fig. S5. Comparison of Auxiliary Cluster 2-encoded Immunity Proteins.** The heat
1190 map illustrates the fraction identity (fraction of identical residues) among core immunity
1191 proteins located in T6SS auxiliary cluster 2 (Aux2) from patient and environmental
1192 isolates used in this study, along with strain representatives of known families [17,61].
1193 Green indicates a fraction identity of 1 (same family and subfamily), yellow indicates a
1194 fraction identity of >0.3 (same family), and red indicates a fraction identity of ≤0.3
1195 (different family). Families are labelled by letters on the side of the heatmap.
1196

bioRxiv preprint doi: https://doi.org/10.1101/2023.10.25.564063; this version posted October 26, 2023. The copyright holder for this preprint (which was not certified by peer review) is the author/funder, who has granted bioRxiv a license to display the preprint in perpetuity. It is made available under aCC-BY-ND 4.0 International license.

1197 **Fig. S6. Comparison of Auxiliary Cluster 3-encoded Immunity Proteins.** The heat
1198 map illustrates the fraction identity (fraction of identical residues) among core immunity
1199 proteins located in T6SS auxiliary cluster 3 (Aux3) from patient and environmental
1200 isolates used in this study. Green indicates a fraction identity of 1 (same family and
1201 subfamily), yellow indicates a fraction identity of >0.3 (same family), and red indicates
1202 a fraction identity of ≤0.3 (different family). Families are labelled by letters on the side
1203 of the heatmap. Dashed lines indicate a longer predicted sequence at the beginning of
1204 the proteins.

1205

1206 **Fig. S7. Comparison of Auxiliary Cluster 4-encoded Immunity Proteins.** The heat
1207 map illustrates the fraction identity (fraction of identical residues) among core immunity
1208 proteins located in T6SS auxiliary cluster 4 (Aux4) from patient and environmental
1209 isolates used in this study. Green indicates a fraction identity of 1 (same family and
1210 subfamily), yellow indicates a fraction identity of >0.3 (same family), and red indicates
1211 a fraction identity of ≤0.3 (different family). Families are labelled by letters on the side
1212 of the heatmap.

1213

1214 **Fig. S8. Comparison of Auxiliary Cluster 5-encoded Immunity Proteins.** The heat
1215 map illustrates the fraction identity (fraction of identical residues) among core immunity
1216 proteins located in T6SS auxiliary cluster 5 (Aux5) from patient and environmental
1217 isolates used in this study. Green indicates a fraction identity of 1 (same family and
1218 subfamily), yellow indicates a fraction identity of >0.3 (same family), and red indicates
1219 a fraction identity of ≤0.3 (different family). Families are labelled by letters on the side
1220 of the heatmap.

1221

bioRxiv preprint doi: https://doi.org/10.1101/2023.10.25.564063; this version posted October 26, 2023. The copyright holder for this preprint (which was not certified by peer review) is the author/funder, who has granted bioRxiv a license to display the preprint in perpetuity. It is made available under aCC-BY-ND 4.0 International license.

1222 **Fig. S9. Comparison of PilA proteins.** The heat map displaying fraction identity
1223 (fraction of identical residues) of PilA from patient and environmental isolates used in
1224 this study, which includes A1552 as a pandemic representative and *V. mimicus*
1225 (ATCC33655) as the outgroup. Green indicates fraction identity of 1, yellow indicates
1226 fraction identity >0.75, red fraction identity >0.5, and dark red fraction identity ≤0.5.
1227 The experimentally proven ability of the PilA variants to self-interact is indicated above
1228 the heatmap.
1229
1230 **Fig. S10. The *pilA* gene likely moves by horizontal gene transfer.** The figure
1231 compared the core gene-based cladogram of the 39 *V. cholerae* strains studied (on the
1232 left side) with the *pilA* nucleotide sequences-based cladogram (on the right side).
1233 Coloured boxes highlight supported clades of relatively related strains, which are also
1234 represented by coloured circles in the *pilA* cladogram. The incongruence between the
1235 genome-based and *pilA* reconstructions suggests horizontal gene transfer of *pilA*. *V.*
1236 *mimicus* (ATCC33655) is used as an outgroup. Statistical significance was verified
1237 using 100 bootstraps, and nodes with bootstrap values below 60 are collapsed.
1238
1239 **Fig. S11. Pilus diversity provides T6SS protection by spatial segregation.**
1240 Microscopy images of co-culture experiments between T6SS-competent (Parent) or
1241 non-functional (Δ*vasK*) predator strains, and T6SS-sensitive (Δ4E/I) prey strains.
1242 Predator and prey strains are either carrying matching (upper panels), or diverse (lower
1243 panels) PilA variants. Phase contrast, a merge of prey (sfGFP, in green) and predator
1244 strains (mCherry, in red), and SYTOX Blue dead cell stain (blue) channels are
1245 displayed. Scalebar indicates 25 μm.
1246

bioRxiv preprint doi: https://doi.org/10.1101/2023.10.25.564063; this version posted October 26, 2023. The copyright holder for this preprint (which was not certified by peer review) is the author/funder, who has granted bioRxiv a license to display the preprint in perpetuity. It is made available under aCC-BY-ND 4.0 International license.

1247 **Fig. S12. Microscopy of strain pairs with promiscuous T4P combinations.** Images
1248 of co-culture experiments between T6SS-competent (predator) and T6SS-sensitive
1249 (prey) strains, displaying all PilA variants, known to exhibit levels of promiscuousness.
1250 Phase contrast, a merge of prey (sfGFP, green) and predator strains (mCherry, red), and
1251 SYTOX Blue dead cell stain (blue) channels are displayed. Scalebar indicates 25 μm.
1252
1253 **Fig. S13. 2D simulations yield a similar phenomenology as 3D simulations.** In
1254 addition to the 3D simulations (see methods section), 2D simulations were performed in
1255 a triangular lattice, with the same division rate, diffusion coefficient, binding energies,
1256 total firing rate, and lysis rate as in the 3D case. The 5 panels show zooms from
1257 snapshots taken after 1 h of 2D simulations where 100x100 triangular lattices were
1258 initialized with 50 prey (green markers) and 50 predators (red markers) placed
1259 uniformly at random (note that this yields a larger density than in our 3D simulations).
1260 Lysing cells are represented by black markers. The black scale bar indicates the length
1261 of 5 marker diameters. On the left: no interaction between prey and predators ($E_{cross} =$
1262 0). The top panel illustrates the complete absence of T4P, while the bottom panel
1263 corresponds to the non-matching T4P case. On the right: prey and predators interact via
1264 T4P with a non-zero binding energy ($E_{cross} > 0$). The top panel shows the matching
1265 T4P case, and the middle and bottom panels correspond to promiscuous T4P, with
1266 E_{cross} equal to $1.5kT$ and $1kT$, respectively.
1267
1268 **Fig. S14. A similar phenomenology is obtained by four variants of the model.** On
1269 the left are 2D simulations, and on the right are 3D simulations. The top panels illustrate
1270 simulations that include the diffusion of aggregates as a whole, while the bottom panels
1271 depict simulations conducted without such diffusion (see methods). All panels show

bioRxiv preprint doi: https://doi.org/10.1101/2023.10.25.564063; this version posted October 26, 2023. The copyright holder for this preprint (which was not certified by peer review) is the author/funder, who has granted bioRxiv a license to display the preprint in perpetuity. It is made available under aCC-BY-ND 4.0 International license.

1272 zooms from snapshots taken after 1 h of simulations performed as described in the
1273 methods section for 3D simulations, and as described in the legend of Figure S13 for 2D
1274 simulations. Prey and predators are represented by green and red markers, respectively,
1275 while lysing cells are represented by black markers. The black scale bar indicates the
1276 length of 5 marker diameters. The main behaviours (aggregation or no aggregation)
1277 remain consistent across all variants of the model. Notably, when aggregates do not
1278 diffuse, multiple prey and predator aggregates are formed after one hour. In contrast,
1279 when they diffuse, aggregates of a particular type coalesce, resulting in a single
1280 aggregate of prey and a single aggregate of predators.

1281

1282 **Fig. S15. Aggregation is facilitated by T4P with sufficient binding energy.** The plot
1283 displays the mean local density, which represents the average fraction of occupied
1284 neighbouring sites of a bacterium, plotted against the T4P binding energy E at steady
1285 state. In this figure, we consider a single type of bacteria (either prey or predators)
1286 diffusing and interacting through T4P with a specific attractive energy E, but without
1287 division or killing. The system can then be mapped to a lattice fluid model, and a Monte
1288 Carlo simulation of its steady state was performed. The blue curve represents the 3D
1289 model where bacteria diffuse on a $40 \times 40 \times 40$ body-centred cubic lattice, and the
1290 yellow curve corresponds to the 2D model where bacteria diffuse on a 100×100
1291 triangular lattice. In both cases, the system comprises 100 bacteria.

1292

1293 Supplementary Tables

1294 **Table S1. Bacterial strains and plasmids used in this study.**

1295 **Table S2. Information on genomes used for bioinformatical analysis.**

1296

bioRxiv preprint doi: https://doi.org/10.1101/2023.10.25.564063; this version posted October 26, 2023. The copyright holder for this preprint (which was not certified by peer review) is the author/funder, who has granted bioRxiv a license to display the preprint in perpetuity. It is made available under aCC-BY-ND 4.0 International license.

1297 ## Supplementary Movies

1298 **Movie S1. Simulation with matching T4P; view of a fixed cube.** This video shows
1299 the evolution of an aggregate over one hour in the case of matching T4P with T6SS
1300 killing enabled. The region of interest is a cube extracted from the full simulation
1301 volume, whose position remains fixed throughout the video. Prey and predators are
1302 represented by green and red markers, respectively. Lysing cells are represented by
1303 black markers. The playback speed of the video compared to real time is indicated at the
1304 top right of the video.

1305

1306 **Movie S2. Simulation without T4P; view of a fixed cube.** This video shows the
1307 evolution of an aggregate over one hour in the case without T4P but with T6SS killing
1308 enabled. The region of interest is a cube extracted from the full simulation volume,
1309 whose position remains fixed throughout the video. Prey and predators are represented
1310 by green and red markers, respectively. Lysing cells are represented by black markers.
1311 The playback speed of the video compared to real time is indicated at the top right of
1312 the video.

1313

1314 **Movie S3. Simulation with matching T4P but no T6SS.** This video shows the
1315 evolution of an aggregate over one hour in the case of matching T4P with T6SS killing
1316 disabled. The region of interest is a cube extracted from the full simulation volume,
1317 centred on an aggregate of interest. However, note that at the beginning of the video,
1318 when aggregates are just starting to form, the aforementioned cube is not centred on any
1319 aggregate yet. Prey and predators are represented by green and red markers,
1320 respectively. Lysing cells are represented by black markers. The playback speed of the
1321 video compared to real time is indicated at the top right of the video.

bioRxiv preprint doi: https://doi.org/10.1101/2023.10.25.564063; this version posted October 26, 2023. The copyright holder for this preprint (which was not certified by peer review) is the author/funder, who has granted bioRxiv a license to display the preprint in perpetuity. It is made available under aCC-BY-ND 4.0 International license.

1322

1323 **Movie S4. Simulation with matching T4P.** This video shows the evolution of an
1324 aggregate over one hour in the case of matching T4P with T6SS killing enabled. The
1325 region of interest is a cube extracted from the full simulation volume, centred on an
1326 aggregate of interest. However, note that at the beginning of the video, when aggregates
1327 are just starting to form, the aforementioned cube is not centred on any aggregate yet.
1328 Prey and predators are represented by green and red markers, respectively. Lysing cells
1329 are represented by black markers. The playback speed of the video compared to real
1330 time is indicated at the top right of the video.

1331

1332 **Movie S5. Simulation with non-matching T4P.**This video shows the evolution of an
1333 aggregate over one hour in the case of non-matching T4P with T6SS killing enabled.
1334 The region of interest is a cube extracted from the full simulation volume, centred on an
1335 aggregate of interest. However, note that at the beginning of the video, when aggregates
1336 are just starting to form, the aforementioned cube is not centred on any aggregate yet.
1337 Prey and predators are represented by green and red markers, respectively. Lysing cells
1338 are represented by black markers. The playback speed of the video compared to real
1339 time is indicated at the top right of the video.

1340

1341 **Movie S6. Simulation with promiscuous T4P.** This video shows the evolution of an
1342 aggregate over one hour in the case of promiscuous T4P ($E_{cross} = 1kT$) with T6SS
1343 killing enabled. The region of interest is a cube extracted from the full simulation
1344 volume, centred on an aggregate of interest. However, note that at the beginning of the
1345 video, when aggregates are just starting to form, the aforementioned cube is not centred
1346 on any aggregate yet. Prey and predators are represented by green and red markers,

bioRxiv preprint doi: https://doi.org/10.1101/2023.10.25.564063; this version posted October 26, 2023. The copyright holder for this preprint (which was not certified by peer review) is the author/funder, who has granted bioRxiv a license to display the preprint in perpetuity. It is made available under aCC-BY-ND 4.0 International license.

1347 respectively. Lysing cells are represented by black markers. The playback speed of the

1348 video compared to real time is indicated at the top right of the video.

(which was not certified by peer review) is the author/funder, who has granted bioRxiv a license to display the preprint in perpetuity. It is made available under aCC-BY-ND 4.0 International license.

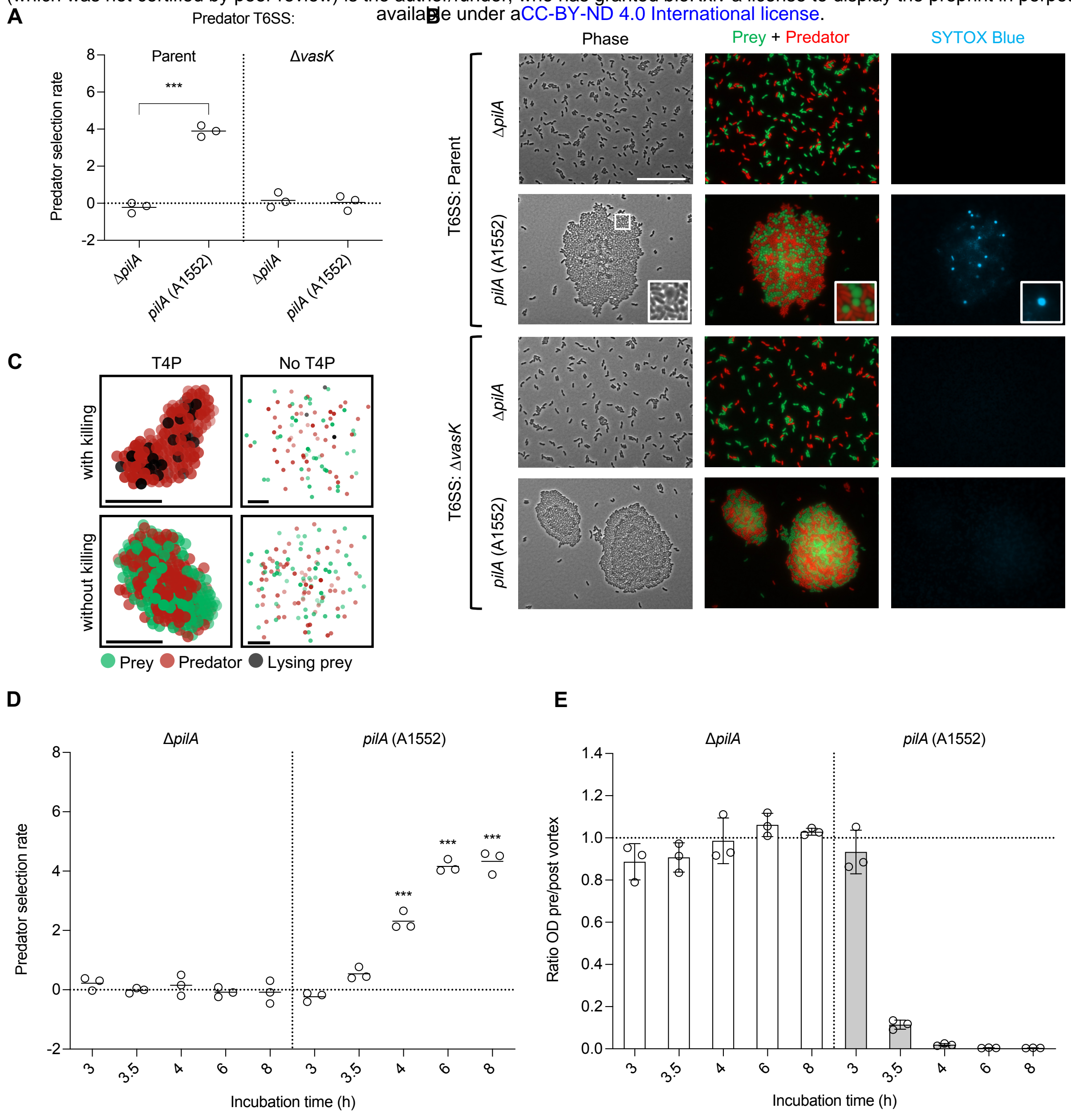

(which was not certified by peer review) is the author/funder, who has granted bioRxiv a license to display the preprint in perpetuity. It is m
available under aCC-BY-ND 4.0 International license.

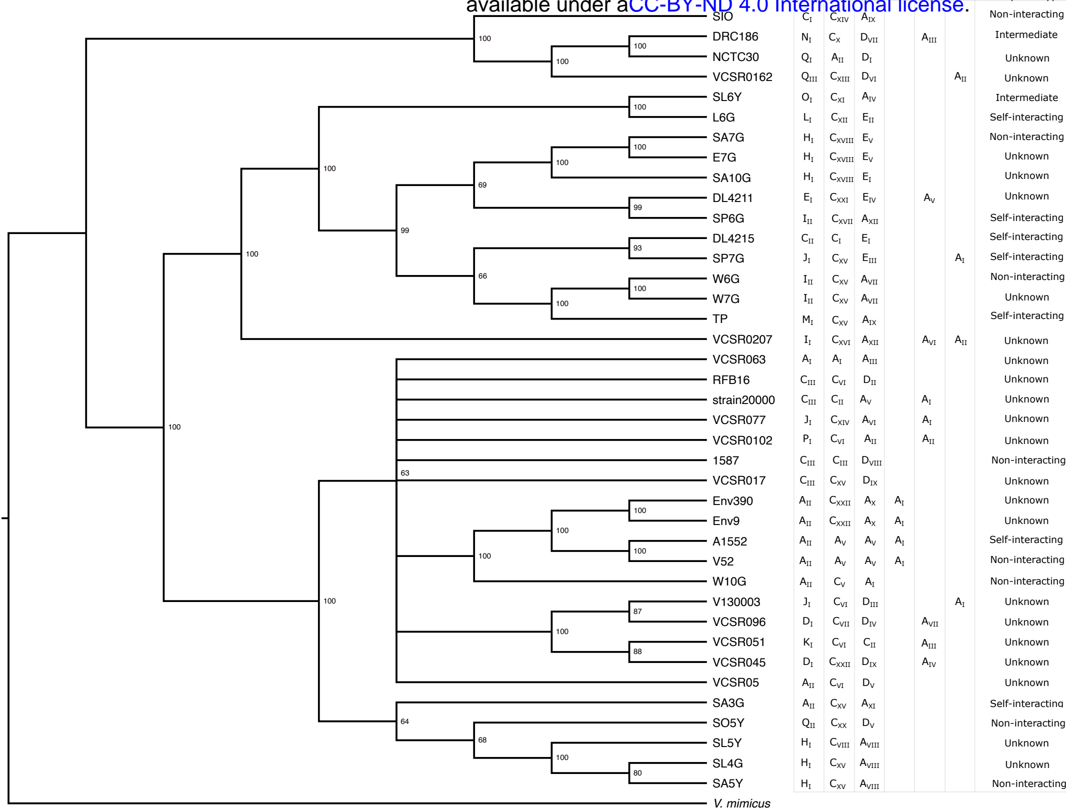

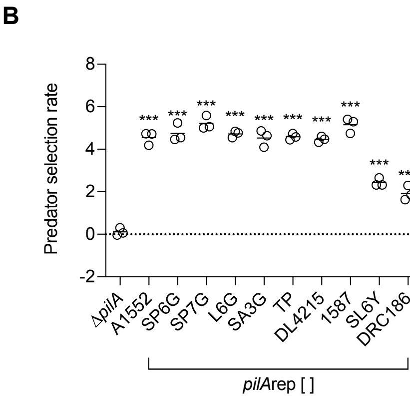

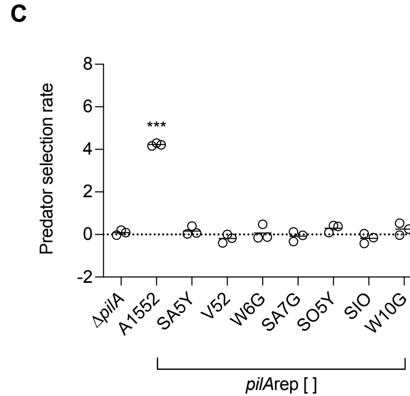

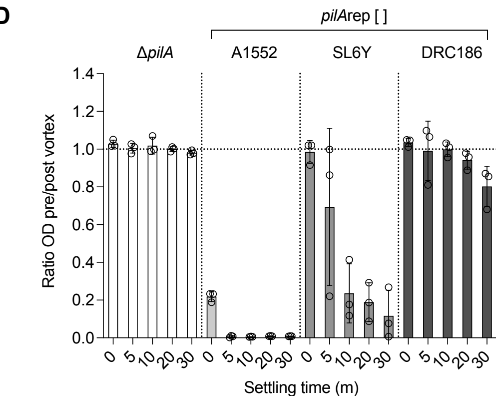

(which was not certified by peer review) is the author/funder, who has granted bioRxiv a license to display the preprint in perpetuity. It is m
available under aCC-BY-ND 4.0 International license.

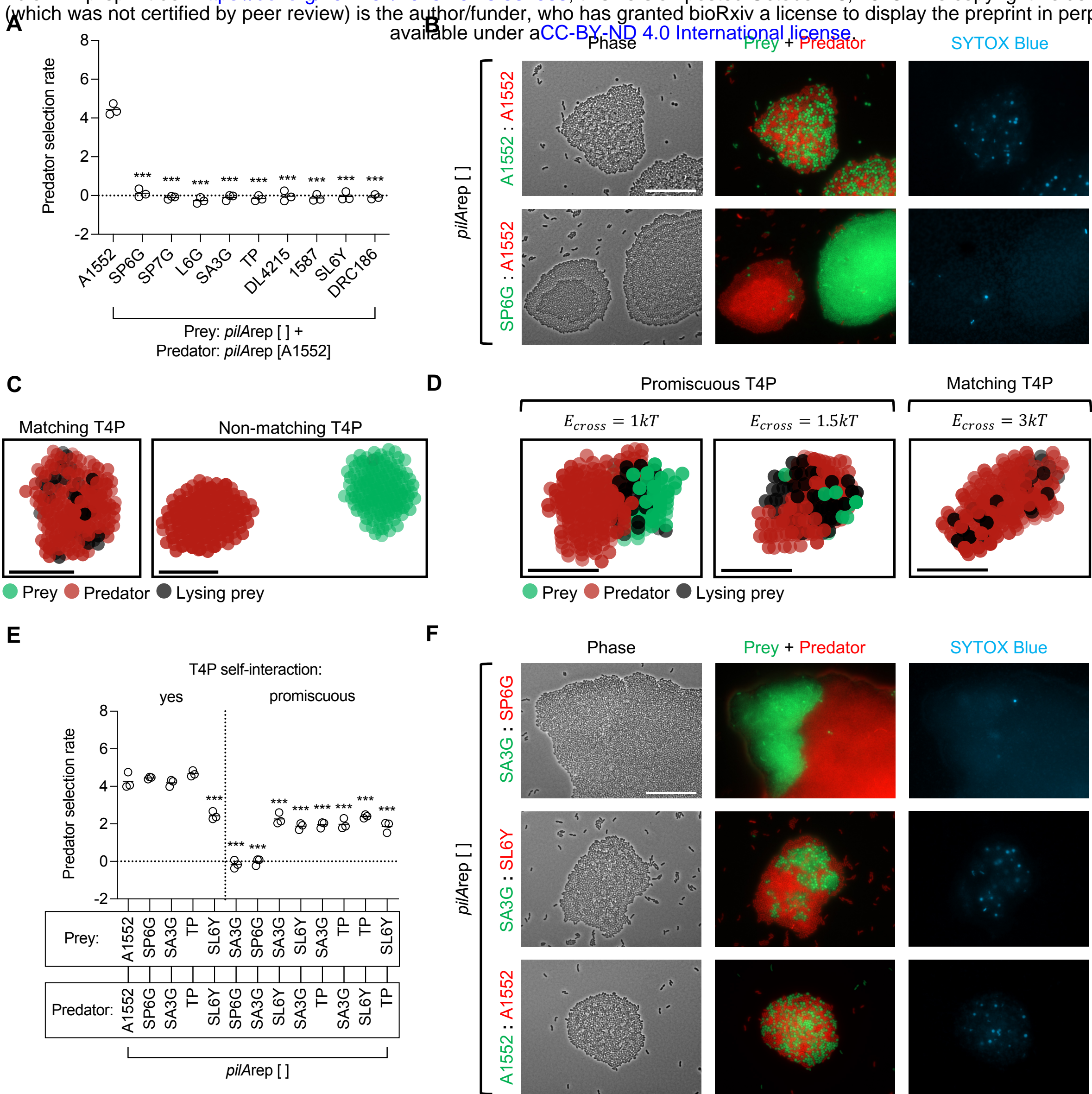

(which was not certified by peer review) is the author/funder, who has granted bioRxiv a license to display the preprint in perpetuity. It is m
available under aCC-BY-ND 4.0 International license.